INVERSE ATTENUATION-FILTERING

A Thesis Submitted to the

College of Graduate and Postdoctoral Studies

In Partial Fulfillment of the Requirements

For the Degree of Master of Science

In the Department of Geological Science

University of Saskatchewan

Saskatoon

By

Mohamed Haiba

PERMISSION TO USE

In presenting this thesis in partial fulfilment of the requirements for a Postgraduate degree from the University of Saskatchewan, I agree that the Libraries of this University may make it freely available for inspection. I further agree that permission for copying of this thesis in any manner, in whole or in part, for scholarly purposes may be granted by the professor or professors who supervised my thesis work or, in their absence, by the Head of the Department or the Dean of the College in which my thesis work was done. It is understood that any copying or publication or use of this thesis or parts thereof for financial gain shall not be allowed without my written permission. It is also understood that due recognition shall be given to me and to the University of Saskatchewan in any scholarly use which may be made of any material in my thesis.

Requests for permission to copy or to make other use of material in this thesis in whole or part should be addressed to:

Head of the Department of Geological Sciences

Geology Building

114 Science Place

University of Saskatchewan

Campus Drive

Saskatoon, Saskatchewan (S7N 5E2)

Canada

Or

Dean

College of Graduate and Postdoctoral Studies

University of Saskatchewan

116 Thorvaldson Building, 110 Science Place

Saskatoon, Saskatchewan (S7N 5C9)

Canada

TABLE OF CONTENTS

LIST OF TABLES

LIST OF FIGURES

LIST OF SYMBOLS & ABBREVIATIONS

A-compensation	Attenuation compensation, Inverse Attenuation-Filtering
2D, 2-D	Two-Dimensional
AGC	Automatic Gain Control
CDP	Common Depth Point (older name for CMP)
CMP	Common Mid-Point
DMO	Dip Move-Out
FWI	Full-Waveform Inversion
F-X	Frequency Space domain
GLI2D	Generalized Linear Inversion in 2D
IGeoS	Integrated GeoScience Software (software package)
NMO	Normal Move-Out
RMS, r.m.s.	Root Mean Square
TWTT	Two-way (reflection) travel time

ABSTRACT

When seismic waves propagate through the Earth, they are affected by numerous inelastic effects of the medium. These effects are usually characterized by the concept of the *Q*-factor and lead to variations of spectra of the signal and shapes of the waveforms, which further affect the results of reflection seismic imaging. Attenuation compensation, also often called the inverse *Q* filtering is a signal-processing procedure broadly used to compensate both of these effects of attenuation in reflection sections or volumes. The objective of this thesis is to present and investigate a new attenuation-compensation approach that is much more general than the conventional inverse *Q* filtering. This approach is based on splitting the attenuation-correction procedure into two parts: 1) modeling of the propagating waveform affected not only by a *Q* but potentially by multiple physical factors within the medium, and 2) time-variant deconvolution of the modeled waveform from the data, also performed by (optionally) using multiple methods. The modeling includes multiple types and frequency dependences of the *Q*-factor as well as possible non-*Q* type effects such as solid viscosity, scattering, wavefront focusing and defocusing, and geometric spreading. The approach is analyzed on application to two real, stacked reflection seismic datasets from China. One of the datasets is a raw 2-D seismic line which I also process in this Thesis to achieve the necessary stacked section. The second dataset from a different area was obtained in already stacked form. In both datasets, application of the inverse attenuation filtering method shows improvements of the waveforms and amplitude spectra of seismic records and increases in seismic resolution. Several types of *Q* and solid-viscosity models are tested. Two approaches to deconvolution are compared, which are the

conventional frequency-domain Wiener deconvolution and a new time-domain approach called the Iterative Time-Domain deconvolution (ITD). The ITD approach achieves particularly good results in terms of improving the resolution of the images as well as the spectra of the records. The tests also illustrate the necessity for spatially smooth attenuation models in *Q*-compensation, which was suggested recently by Morozov and Baharvand Ahmadi (2015).

ACKNOWLEDGEMENTS

First and foremost, I would like to thank Allah Almighty. My thesis would not have been existing without Allah's blessing.

I would like to express my very great appreciation to my supervisor, Dr. Igor Morozov, for his guidance and motivation to complete this thesis. He has been fully supportive, patient and caring in and outside the academic work. I am gratefully indebted to his for his very valuable comments, suggestions, and knowledge. I also want to extend my gratitude to the members of my supervisory committee: Dr. Samuel Butler and Dr. James Merriam, and the external examiner Dr. Christopher Hawkes. Many thanks also to Chantal Strachan-Crossman, who is our Graduate Program Administrator. My deep appreciation goes out to all students, staff, and faculty at the Department of Geological Sciences of the University of Saskatchewan.

I am really thankful and grateful for the opportunity and the effort from my supervisor that helped me to learn and use some powerful and great software such as ProMAX, GeoTomo, and IGeoS. In addition, I thank Song Hu for always offering quick and motivated help with any problems or issues with the software. I gratefully acknowledge the support from the NOC (National Oil Corporation Libya).

I express my gratitude to my current and previous officemates Osama El Badri, Kamal Abo Jnah, Maryam Safarshahi, Wubing Deng, Yichuan Wang, my friends Moji and Renaud. I would like to express my deepest gratitude to my friend and brother Yousef Khanfas for his support and standing by me in the bad and good time. Special thanks should be given to Nancy

Williams for being a warm heart and her motivation for me in each and single time I see her, and of course I thank her for her delicious food that she makes in every special occasion.

Last but not least, I would like to express my huge thanks and deepest appreciation to my wonderful family. To my father Abdulwahab Heba, my most important person in the world; my mother Faeza, my brother Ahmed, my sisters Nada, Izdehar and her kids (Mohamed, Assal, Abu Bakr, Omar), and my brother in law Seddiq for his support and taking care of my family while I am away. I thank them all for their support, motivation, and unconditional love. They are currently living in a war zone, but whenever I call them, they always try to make it feel like it is nothing just to make me feel that they are safe and provide positive energy. Thank you very much for being my family I will always be indebted to.

CHAPTER 1

INTRODUCTION

Reflection seismic imaging is one of most effective methods for studying the interior of the Earth, particularly for the purposes of oil and gas exploration. Reflection imaging produces high-resolution images of large zones within the Earth's subsurface, which are very important for geological interpretations. However, there are several limiting factors reducing the quality of reflection seismic images, which are the effects of the source, variabilities of the shallow subsurface near receivers, path effects, and various types of noise. In this study, I focus on one of these factors related to path effects of the medium on seismic waveforms. These factors represent the phenomenon of seismic attenuation.

Seismic waves propagating through the Earth subsurface are almost always affected by the inelasticity of the medium. In this Thesis, I do not consider the physical mechanisms of inelasticity but rather focus on its effects on the waveforms and on the ways these effects can be corrected for. Generally, attenuation effects cause amplitude decays in the propagating wave and a corresponding distortion of the seismic waveforms. In order to produce high-resolution seismic images, it is necessary to remove these attenuation effects, thereby recovering the true shapes and amplitudes of the waveforms. There exist several techniques for reducing the attenuation effects in seismic records, such as the inverse *Q*-filtering (*Q*-compensation) and several types of spectral transformations of the signal. These methods are based on the viscoelastic (based on the concept of the quality factor, or *Q*). A brief discussion of this concept and a summary of *Q*-based attenuation models are given below in this Chapter.

In this study, I contribute to the development, investigate, and test a novel broad approach to inverse *Q*-filtering, which corrects not only for the *Q*-based, but also other models of seismic attenuation. By analogy with *Q*-compensation but with a much broader approach to seismic attenuation and inversion (deconvolution), the new method is called attenuation-compensation, or *A*-compensation by Morozov et al. (2018) and in this thesis. *A*-compensation is a broad concept consisting of forward modeling of the propagating source waveform followed by inverse filtering, with options for using a variety of modeling and deconvolution algorithms depending on the properties of the acquired data. This approach is significantly more general than inverse *Q*-filtering, makes fewer assumptions and offers a range of options for modeling various types of attenuation mechanisms.

In this Chapter, I describe the general concept of seismic attenuation and its correction in seismic records (section 1.1), summarize the objectives of this Thesis (section 1.2), and outline its structure (section 1.3).

1.1 Problem Overview

All inelastic media absorb energy from propagating waves. Seismic attenuation is caused by various physical properties of the medium and greatly complicates the study of reflection seismology. Wave attenuation features in fractured and weathered zones, in rock saturated with fluids, in partial melts, and in hydrocarbon reservoirs. All of these factors cause a significant amplitude loss, velocity dispersion and phase distortions of the waveforms (Zhou et al., 2011). An example of attenuation in gas reservoirs is the amplitude loss due to gas chimneys, which

occur when gas diffuses through a fracture system into the surrounding area of the reservoir. This process creates an inhomogeneous gas-saturated zone which results in an inhomogeneous velocity field, causing distortion of the seismic waveforms (Arntsen et al., 2007).

Attenuation-related properties of the wavefield are usually described by the *Q* factor. Knowledge of the *Q* factor is very important, and several types of measurement techniques exist based on using direct waves, reflections, coda observations (in earthquake seismology), and ultrasonic and seismic-frequency laboratory experiments. However, direct measurement of *Q* is a large and complicated subject, which lies outside of the scope of this Thesis.

Generally, seismic attenuation is inversely proportional to *Q*. Dry rocks are characterized by a high *Q* (low attenuation) whereas fully liquid-saturated rocks have a low *Q* (high attenuation) (Aki and Richards, 2002; Li et al., 2006). The amplitude decay of a propagating waveform as a function of angular frequency ($\omega = 2\pi f$) and propagation time (t) can be described as:

$$A(\omega, t) = A_0 e^{-\frac{\omega t}{2Q}}, \tag{1.1}$$

where A_0 is the amplitude at time $t = 0$, ω is the angular frequency, Q is the apparent quality factor of the propagation path. The inverse Q factor is defined as the ratio of the energy loss ΔW per cycle to the peak elastic energy W.

$$\frac{1}{Q} = \left(\frac{1}{2\pi}\right)\frac{\Delta W}{W}. \tag{1.2}$$

One key characteristic of seismic attenuation is that high-frequency waves tend to attenuate faster (reduce in amplitude with propagation distance) than the low-frequency ones. Amplitude decay (1.1) can also be described as a function of travel distance $x = Vt$, as

$$A(\omega, x) = A_0 e^{-\alpha x}. \tag{1.3}$$

In the above, the spatial attenuation coefficient, α, generally increases with frequency and models the various physics, including: intrinsic attenuation, reflectivity (elastic scattering), and geometrical spreading. The attenuation coefficient can be further separated into zero-frequency and frequency-dependent parts. It can be related to Q and the phase velocity, V, of the propagating wave as:

$$\alpha = \left(\frac{\omega}{2V} \right) \frac{1}{Q}. \tag{1.4}$$

Here, the phase velocity is related to ω as:

$$V = \frac{\omega}{k}, \tag{1.5}$$

where $k = 2\pi/\lambda$ is the wavenumber, and λ is the wavelength. In the presence of attenuation, k is not simply proportional to ω, and consequently V is frequency-dependent Figure 1.1 (Aki and Richards, 2002). This dependence $V(\omega)$ is called the phase-velocity dispersion, and it is responsible for deformation of the waveform.

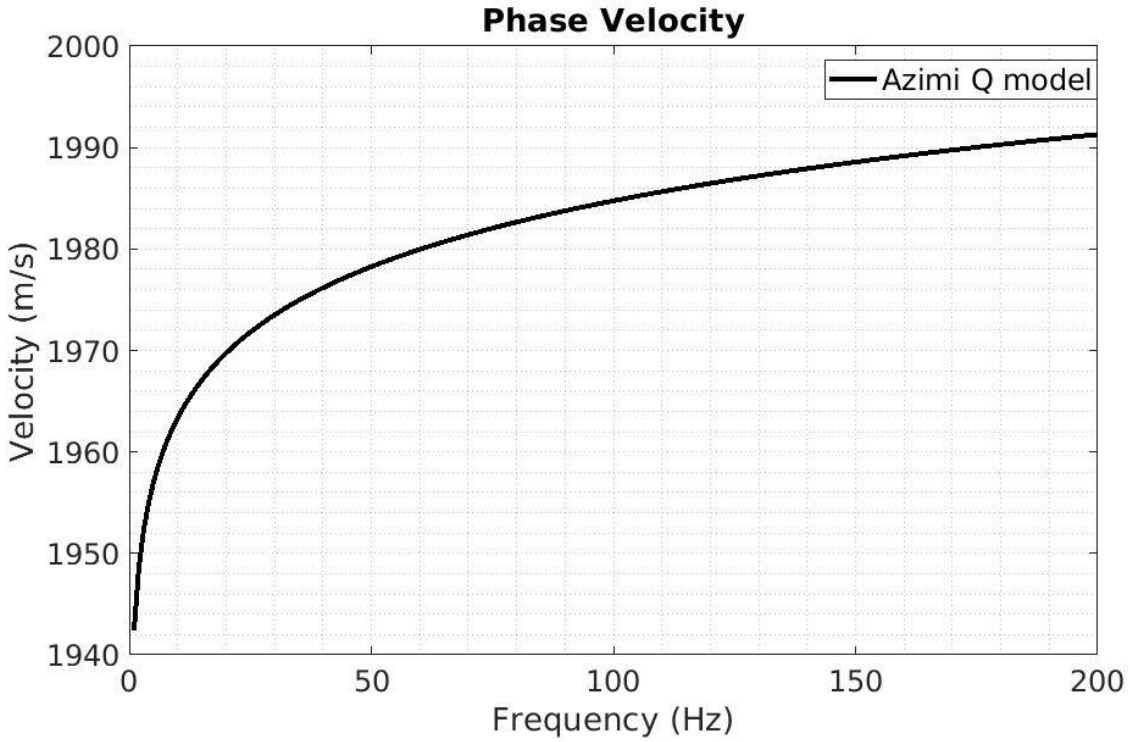

Figure 1.1 Velocity dispersion and frequency relation using Azimi *Q* model

Measurement of seismic attenuation are usually achieved by using one of several methods to estimate *Q* factor. One of the most commonly used techniques for *Q* estimation is the spectral-ratio method. In this method, the *Q* factor is evaluated by fitting a straight line to the logarithm of spectral ratio over a finite frequency range:

$$\ln\left(\left|\frac{A_2(f)}{A_1(f)}\right|\right) = \ln\left(\frac{g(t_2)}{g(t_1)}\right) - \frac{\pi f (t_2 - t_1)}{Q}, \tag{1.6}$$

where A_1 , A_2 are the amplitude spectra of the traveling wave at two different times t_1 and t_2 and $g(t_1)$ and $g(t_2)$ are the geometric spreading factors at these times. If the negative slope of this

linear dependence is denoted $k = \partial \ln\left(\left|\frac{A_2(f)}{A_1(f)}\right|\right) \Big/ \partial f$, then the Q can be estimated as:

$$Q_{estimation} \approx -\frac{\pi f (t_2 - t_1)}{k}. \tag{1.7}$$

Measurements of the values of Q and the attenuation coefficient α provide important information about the subsurface such as subsurface lithology, presence of melts, or gas and fluid saturation. The determination of Q is the necessary starting point for the process of inverse attenuation filtering. Only once we know Q, we can effectively correct for the detrimental effects of Q such as amplitude decay, phase distortion and scattering.

Within the general attenuation phenomena, the elastic and inelastic effects are usually differentiated. To differentiate them, we need to consider the general underlying physics of energy dissipation. First, elastic phenomena conserve the total mechanical energy of the wavefield but redistribute it in time and space, so that the measured wave amplitudes are diminished. This elastic attenuation (and Q) broadly includes geometrical spreading/multi-pathing, focusing/defocusing, reflectivity due to layered media, and elastic scattering. By comparison, inelastic phenomena involve transformations of the mechanical energy of the wave into heat. These mechanical-energy losses can be due to mechanical friction, such as grain-boundary sliding, or viscosity of pore fluids within the rock, or to non-mechanical phenomena such as temperature variations, heat flows, electrical or magnetic interactions.

Elastic-attenuation factors such as geometrical spreading are often corrected prior to Q measurements, and consequently, it is often assumed that the measured Q is the intrinsic

(inelastic) *Q*. However, elastic effects caused by short-scale heterogeneities of the velocity/density structure can extremely complex and impossible to model completely (Morozov, 2010). Therefore, elastic effects are typically calculated using simplifying assumptions such as uniform velocity models and straight rays. The remaining uncorrected-for elastic effects are then included in the so-called "scattering *Q*". Therefore, the corrections for geometric-spreading effects often affect the *Q* values derived by several types of measurements (Morozov, 2008, 2010). This trade-off of *Q* with geometric spreading and scattering is particularly strong in earthquake seismology, where frequency-dependent $Q(\omega)$ values are often observed (Morozov, 2008). In cases where the size of heterogeneity is too small to be modeled as elastic (geometrical-spreading) and too large for to be modeled as scattering, the resulting *Q* can be highly variable; a so-called "fluctuation *Q*" (Morozov and Baharvand Ahmadi, 2015). These questions of the uniqueness, trade-off with elastic structures, and apparent character of *Q* are very complicated and are outside of the scope of this Thesis. In this study, instead of considering the physical meanings of the *Q*, I treat the *Q* as an apparent, intermediate property, which is measured empirically. This *Q* can be modeled by a variety of physical approaches and algorithms, but details of these algorithms are insignificant for *A*-compensation (Morozov et al., 2018).

Depending on the specific physical mechanism, wave attenuation is always associated with some form of wave-velocity dispersion. Dispersion has a great impact on changing or distortion the shape of wavelet. In conventional seismic processing procedures, velocity dispersion is often omitted due to the lack of insufficient observations. This simplification,

however, sometimes causes losses of the seismic information and sometimes leads to artefacts in seismic images.

Historically, in practical work with seismic records, and in the viscoelastic theory, it is usually assumed that the P-wave and S-wave *Q*-factors *(*Q_P and Q_S) are some effective properties of the medium (Wang, 2008). These *Q*s are assumed to be the same for different waves within medium: for traveling body waves, surface waves, or standing waves. However, the above arguments and also Morozov and Baharvand Ahmadi (2015) show that more precisely, *Q* is only an apparent (or measured) property of the given wave propagating through the medium or of an oscillation of a finite body. This property depends on the way by which the attenuation is measured. For example, the *Q* factor of a sandstone cylinder depends on whether its surface is insulated or permeable for pore-fluid flow (Dunn, 1987). However, and fortunately for the present project, knowledge of this apparent *Q* is sufficient for correcting for attenuation effects (Morozov et al., 2018). In this Thesis, I will first utilize several alternate models of physical mechanisms to produce apparent *Q* factors and further use these modeled *Q* factors to perform attenuation corrections.

1.2 Objectives of this Thesis

In this study, I focus on removing attenuation effects in real seismic reflection data by using the procedure of "Inverse attenuation-filtering" or "*A*-compensation", which is a generalized approach to attenuation corrections which we proposed recently (Morozov et al., 2018). This approach performs corrections for attenuation effects by forward modeling of a

propagating waveforms and applying several types of inverse filtering algorithms. My general goal in this Thesis consists in comparative analysis of different modeling and deconvolution algorithms and making recommendations regarding their applications to the data. The art of determining the *Q* values for real or synthetic seismic data is an ongoing area of research which lies beyond the scope of this study.

The specific objectives and data analysis steps of the present study include:

1) Preparation and processing of the stacked seismic section used an input in the inverse *A*-compensation method. This step involves a complete cycle of standard reflection processing with additional consideration for noise reduction and for the preservation of true amplitudes.
2) Application of the *A*-compensation method to two seismic data sets. The first of these data sets is already stacked, and therefore the application of *A*-compensation to it focuses on demonstrating and testing the attenuation-correction method. The second data set is a raw, pre-stack 2-D seismic line in which I also perform a complete reflection processing and data analysis.

1.3 Structure of this Thesis

In the present Chapter, I give a brief introduction about seismic wave attenuation and its effects on seismic reflection images. At the end of this Chapter, I outline the objectives of this project.

In Chapter 2, I describe the seismic data and processing performed on the second (pre-stack) dataset of this study. With respect to the main objectives of this study, this is a preparatory work; however, it requires substantial effort using a variety of reflection-data approaches and solving a number of problems related to these particular seismic data. In addition to standard data processing, I describe several filtering procedures aimed at reducing the surface wave noise in the data set to get a satisfying seismic section. The final processed seismic section will be the input for inverse attenuation-filtering in Chapter 4.

In Chapter 3, I present the theory of forward and inverse attenuation-filtering and describe the technique of *A*-compensation (inverse attenuation-filtering). In addition, in this Chapter, I discuss several attenuation mechanisms and *Q* models. Finally, I introduce several deconvolution methods for inverse attenuation-filtering, particularly emphasizing the Wiener and iterative time-domain deconvolution methods that are used in further applications.

In Chapter 4, I illustrate applications of several forward modeling and *A*-compensation approaches on the two data sets of this study. These illustrations are conducted for several types of attenuation models.

In Chapter 5, I summarize the conclusions and offer recommendations for future research.

CHAPTER 2

SEISMIC DATA PROCESSING

The inverse attenuation filtering and data analysis in this Thesis are performed by using two seismic datasets provided by a Saskatoon-based company called PanImaging Software Development Limited (http://www.panimaging.com). At the early stages of this project, this company expressed interest in the attenuation-compensation research and software and provided the test data for this study. One of these test datasets is a two-dimensional (2-D), 9.8 km long stacked seismic line, and the other dataset was received in pre-stack form. Both datasets were acquired in western China, but geographic locations and geological details were not disclosed to us. Some of the acquisition details important for data processing will be discussed later in Chapter 2 and Chapter 4.

Before applying inverse-attenuation filtering, the seismic data need to be completely processed to the form of stacked images. In principle, *A*-compensation should be applicable to pre-stack reflection as well as other (refraction, earthquake) data, but I only consider the stacked (single-trace reflection) applications in this Thesis for simplicity, similar to most other applications of *Q* compensation. However, pre-stack applications should still be considered in future research. For the stacked dataset examples used in Chapter 4, only filtering spectral analysis, and *f-x* deconvolution was required in order to analyze the image quality and effects of attenuation corrections. For the pre-stack dataset, complete processing was required, which is described in the present Chapter. In sections 2.1 to 2.5, I describe key processing procedures and preview the results.

I processed the pre-stack PanImaging dataset by utilizing ProMAX software to produce a final seismic section, which was further used in the inverse-attenuation filtering applications. Several data processing procedures are required in order to produce a high-quality seismic section suitable for inverse attenuating-filtering process. Some of these processing steps are standard in reflection seismic processing, and some of them are optional depending on the quality of the acquired data and final goals of processing. Table 2.1 summarizes the processing sequence for the pre-stack seismic dataset.

Table 2.1 Seismic data processing sequence

SEG-Y data input
2D Geometry assignment and trace editing
First arrival picks (First break)
Velocity model and total statics for shots and receivers
Ground roll filtering
Velocity analysis
Normal move out corrections
Brute CMP stack
Residual statics corrections
Dip move out corrections
Redo velocity analysis
Normal move out corrections
CMP stack
F-X deconvolution

In the following sections, I describe six selected steps of this procedure in more detail. These steps are the most essential for improving the data in terms of reducing the noise, increasing signal to noise ratio, collecting important information such as velocities, and producing a final stacked seismic section

Table 2.2 Key geometry parameters

Number of shots	216
Number of receivers	834
Numbers of CMP	1268
Average CMP spacing	12.5 m
Average receiver spacing	25 m
Record length	2200 ms
Number of recording channels	400
Shot hole average depth	25 m
Sample interval	2 ms
Maximum CMP fold	105
Maximum offset	5061 m

2.1 Preprocessing and Picking First Arrivals

The initial preparation of pre-stack dataset is a time-consuming procedure consisting of preprocessing (creation of geometry database, binning, trace editing, and quality control) and picking first arrivals). Geometry assignment is a process creating an accurate description of the field geometry and tying this geometry information to the data traces. This operation is one of the most important steps in any seismic data processing. Geometric accuracy is critical for

processing the data and obtaining interpretable seismic images. Two-dimensional (2-D) geometry assignment provides the geographical reference of our data. Geometry parameters are used in many processing steps described below.

Geometry data for the pre-stack seismic line were imported from three types of SPS (Shell Processing Support) files: the so-called S file (for shot points), R (for receiver groups), and X (for shot-receiver relation records). These data were input into the ProMAX geometry database. Geometry assignment was followed by CMP (common mid-point) binning. The resulting binned dataset contains 1200 CMPs. Figure 2.1 shows the resulting CMP fold distribution in the dataset.

Figure 2.1 CMP fold coverage for the binned dataset. The maximum obtained CMP fold (top of the plot) is 105.

As Figure 2.1 shows, within the middle about one-third of the line (from CMP 880 to about 1400, the CMP fold is near-constant and equals about 96, and outside of this range, the fold linearly reduces toward the ends of the line.

First-arrival (direct- and head-wave, or first-break) picking is a processing step essential for building the initial velocity model for the near surface and determining static corrections. I performed first-break picking by using the GeoTomo software. In this procedure, there are several options for achieving consistent picking, such as selection of the peaks, troughs, or zero crossings for picking or applying AGC (Automatic Gain Control) for improved displays.

After finishing the first-break picking, I calculated the reciprocal travel-time errors Figure 2.2. Reciprocal points within a seismic dataset are such that the source and receiver locations in one shot are approximately equal the receiver and source locations, respectively, for the second shot. Figure 2.2 b) shows the depth variation of the shots and receivers. The shot depth varies along the profile from 5m to 20m.

By the fundamental principle of reciprocity (reversibility of wave propagation), the first-arrival times for reciprocal records should be equal regardless of the subsurface structure and seismic velocities. Wherever reciprocal-time mismatches were found, I reviewed and revised the picks for each shot so that no more than 20 ms of average reciprocal errors were obtained in it. The reciprocal-error test (Figure 2.2c) helped ensuring consistent picking of multiple shots and obtaining a reliable initial velocity model. The principle of reciprocity suggests that the travel time of a seismic wave is independent of the propagation direction, so that if we switch the source and receiver positions, the travel time should be the same. The reciprocal error calculates

the time difference when we switch the direction of the traveling waves. Mismatches between reciprocal times often indicate errors in shot coordinates or effects of near-surface velocities above the sources, such as uphole times. In the process of checking reciprocal times, I had to reject one shot from the dataset because it resulted in reciprocal-time errors greater than 20 ms.

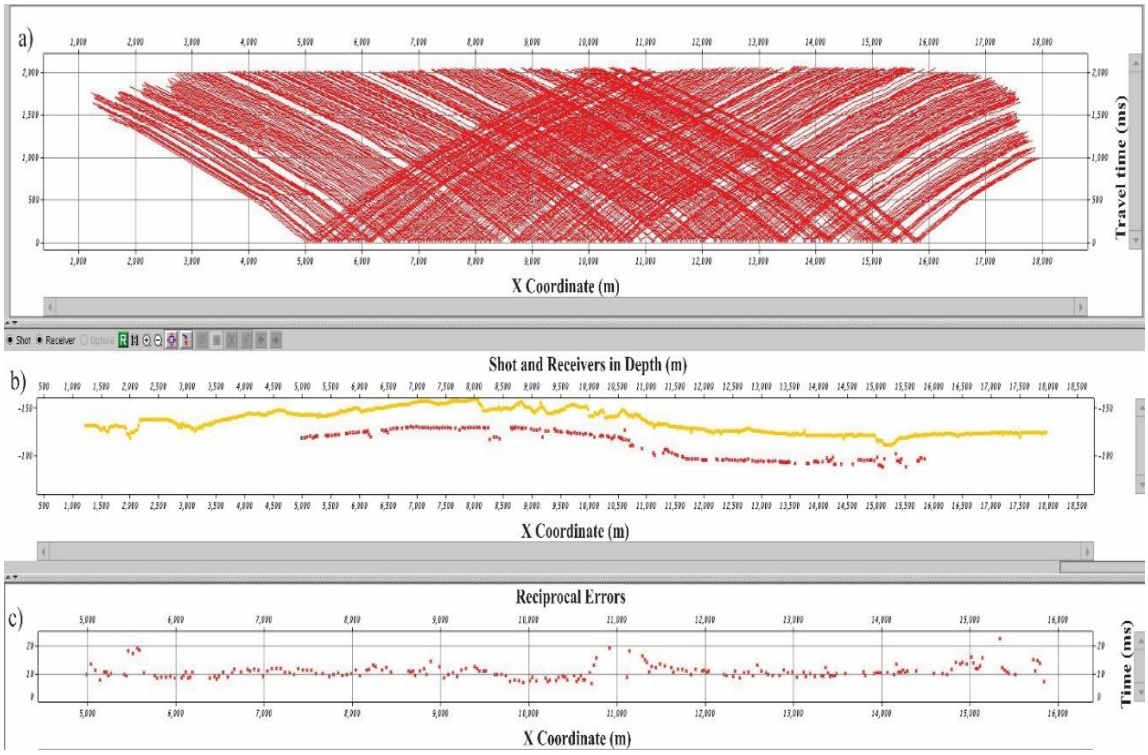

Figure 2.2 First-arrival travel-times: a) Displays the first arrival time picks for all shots; b) elevation of the shots (red), and receivers (yellow). c) reciprocal errors calculated at each receiver

2.2 Refraction velocity Model and Static corrections

Following the first-break picking in ProMAX, the picked travel times were transferred into the GLI2D program by Hampson-Russel (currently included in GeoTomo software). This

program was used to calculate the statics for all sources and receivers and to build the weathering layer model. Within GeoTomo, I started building the initial velocity model by defining three control points and creating an initial 1-D velocity model. The 1-D models were obtained by identifying the refracted arrivals and measuring their intercept times and moveouts. Figure 2.3 shows all of the first-break picks together with the control points (red diamonds). I chose as indicating the changes in the time-distance slopes (moveouts).

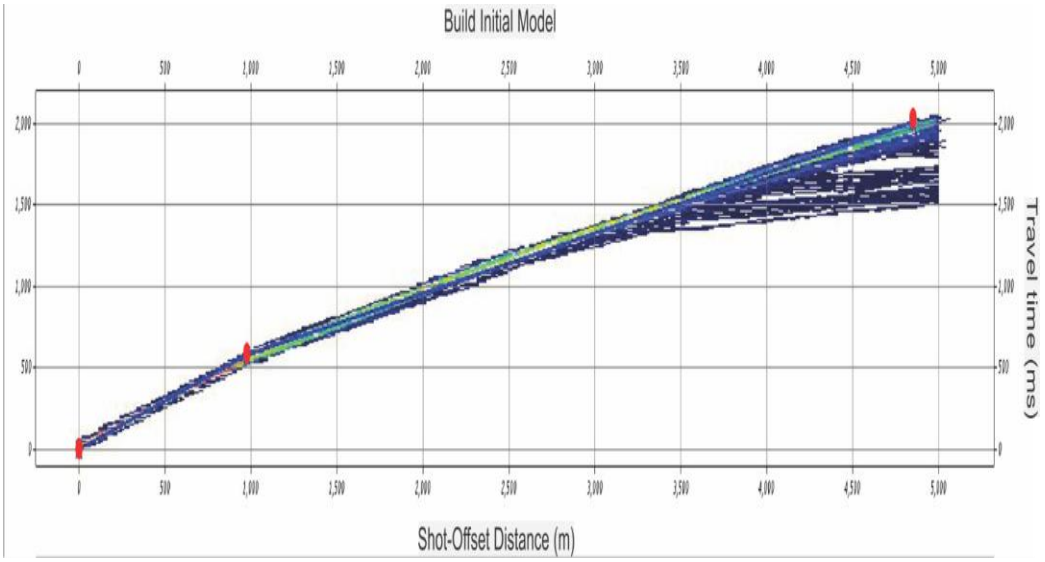

Figure 2.3 Travel time display in offset domain. The three red circles show the ends of near-linear segments of travel-time curves

From these changes of moveouts, I determined that my initial model should include two layers. By using these initial models as input for program GLI2D and making 10 iterations of velocity tomography, I obtained the final velocity model shown in Figure 2.4.

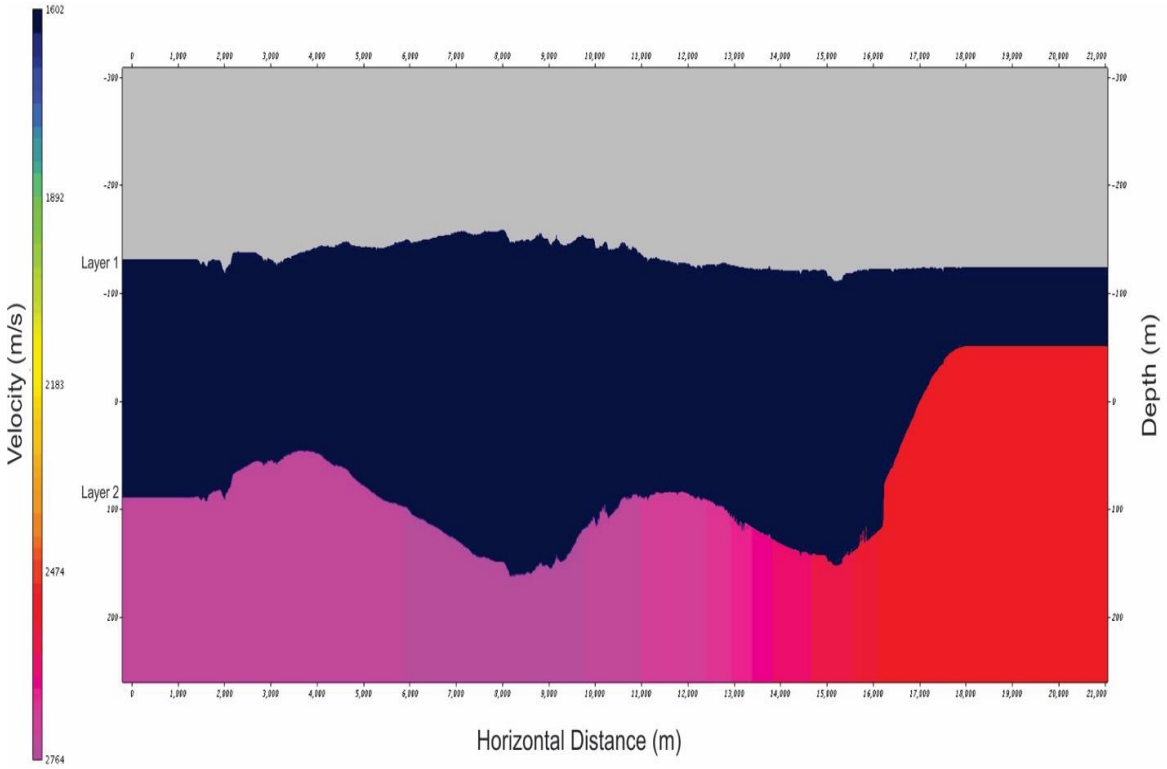

Figure 2.4. Final near-surface velocity model.

Figure 2.4 shows the resulting 2-D refraction velocity model. In this model, the near-surface velocities range from 1602 m/s (top layer) to 2764 m/s (bottom layer). The second model layer has a horizontal velocity variation (shown by the color bar), and the boundary has some steep changes of depth. By evaluating travel times for rays crossing this model vertically, static terms were evaluated for subsequent reflection data processing.

By using the near-surface velocity model (Figure 2.4), the receiver and source statics were calculated by using GeoTomo tools. After this, I calculated the total statics for both receivers and sources by using the obtained near-surface model, floating datum, intermediate

datum, and the replacement velocity. Figure 2.5 shows the static calculation results. The time shifts of the sources and receivers are similar and vary from –60 to –10 ms. As expected, the general trend of those time shifts follows the topography of the area.

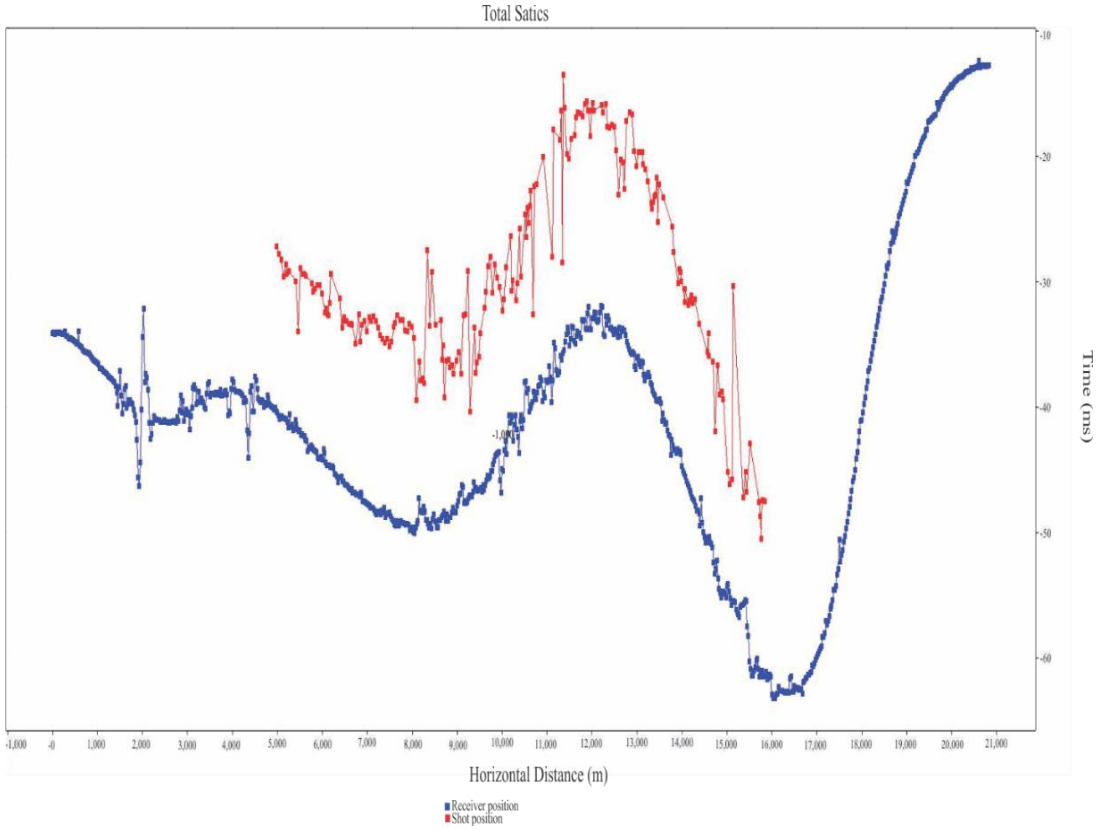

Figure 2.5 Calculation of refraction statics. Values of statics for receivers (blue) and sources (red)

Static corrections performed to remove the irregularities in the near surface. These irregularities affect the reflections time of the subsurface and distort their hyperbolic shapes. Removing this distortion of the reflectors time is done by decreasing the source and receivers lowering the position of the receivers and sources vertically to a datum below the weathering

layer. By applying these static shifts to seismic data, shots and receivers were relocated from their original positions: first, to the intermediate datum by using the velocity field associated third, to the final flat datum. These relocations were performed by subtracting the corresponding static time corrections from the times of the records with the near-surface area; second, to the floating datum by using the replacement velocity; and

2.3 Ground Roll Filtering

Ground roll in seismic sections consists of recordings of high-amplitude, large-moveout, low-frequency surface waves, which often have strong detrimental effects on the resulting images. In attempting to remove the surface wave from the pre-stack dataset, I tried two techniques, both of which produced satisfactory results.

The first method consisted in applying a zero-phase band-pass filter with carefully selected low-cut ramp frequency of 15 to 20 Hz. Figure 2.6 shows a comparison of one shot before (right panel) and after (left panel) removing the ground-roll by utilizing an Ormsby band-pass filter. The red circled area indicates the ground-roll which is removed on the left side plot. This shows that the band-pass filter is successful in removing both the ground-roll and other noise in the presented shot gathers.

In the second technique for ground-roll reduction, I applied the so-called radial transform to the dataset. The radial trace transformation transforms the data into the so-called radial domain (lines of constant moveouts in a shot gather), so that the coherent noise with a particular (low for ground roll) velocity can be filtered out by ordinary band-pass filtering or muting of the

constant-moveout records. The radial transform is a geometric repositioning of trace amplitudes from offset axis to velocity axis by linear interpolation which represent linear apparent velocity. After filtering, inverse radial transform is applied to convert the data back to the original form in the time-space domain, with coherent noise reduced.

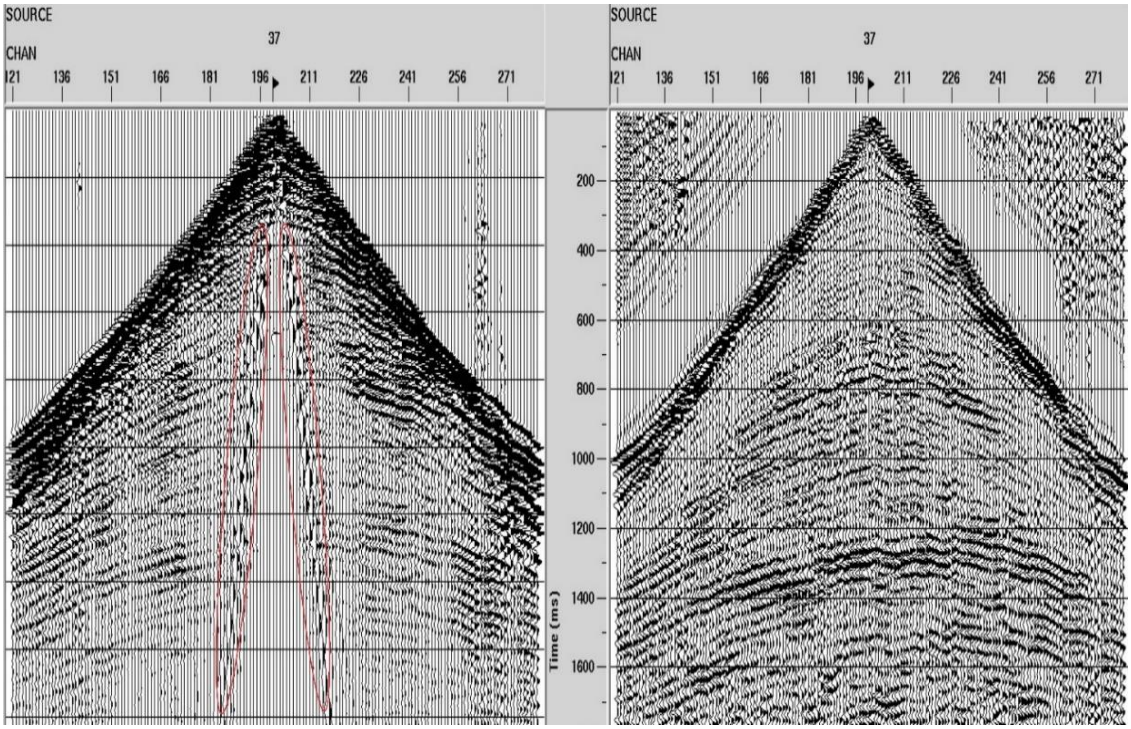

Figure 2.6 Comparison of a shot record before (left panel) and after (right) applying a band-pass filter. The ground-roll (red circled area) has been removed significantly after applying the filter

Figure 2.7 illustrates forward radial-transform before (top) and after frequency filtering (bottom) of one shot gather in the pre-stack dataset of this study. After the transform, the ground roll is confined to a narrow range of traces near the middle of the section, indicated by the ellipse in Figure 2.7 (upper plot).

These ground-roll waveforms are of much lower frequency than in the original input record. Therefore, the ground-roll signals are effectively removed by a low-cut filter while retaining the reflection signal as shown in Figure 2.7 (bottom plot)

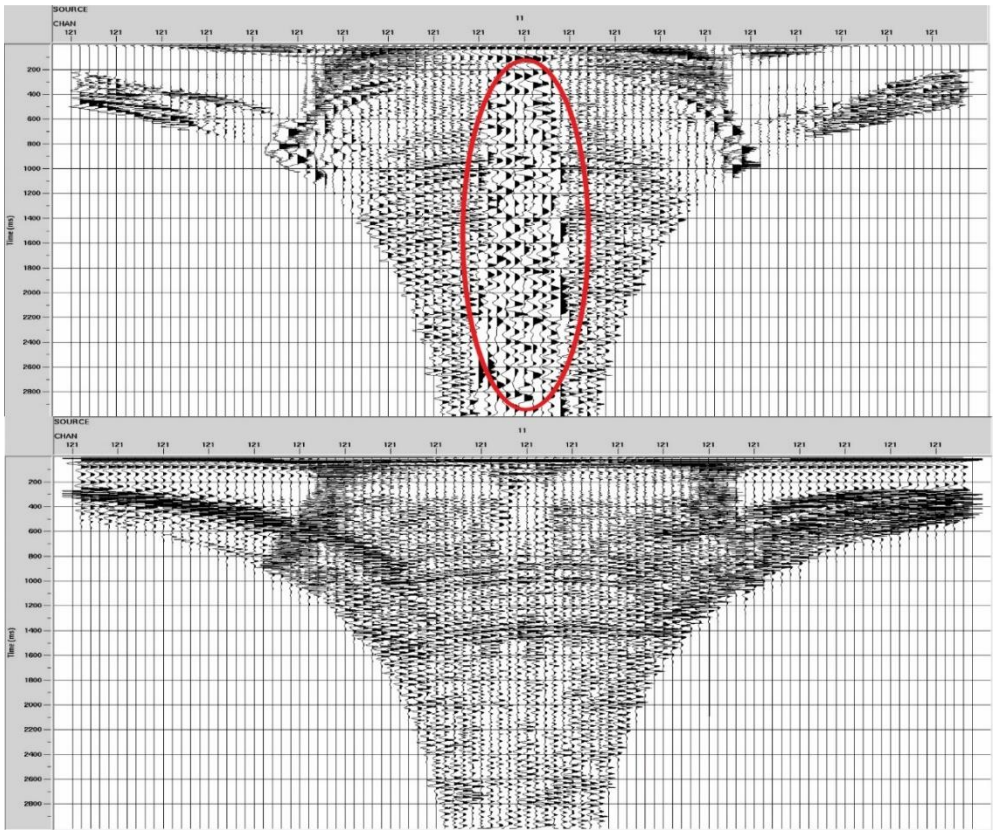

Figure 2.7 Radial transform applied to one shot record. Ground roll (surface wave) is indicated by the red circled area.

After removing the ground roll, an inverse radial transform was applied to transform the dataset back to time domain Figure 2.8 (right panel). Note that the result is similar to the result using the first technique to remove the ground-roll. When applying the inverse radial transform, some artifacts arose in two shot gathers, but the overall results of radial transform filtering are

promising and show a better result than Ormsby band-pass filter in some shot gathers among the entire dataset.

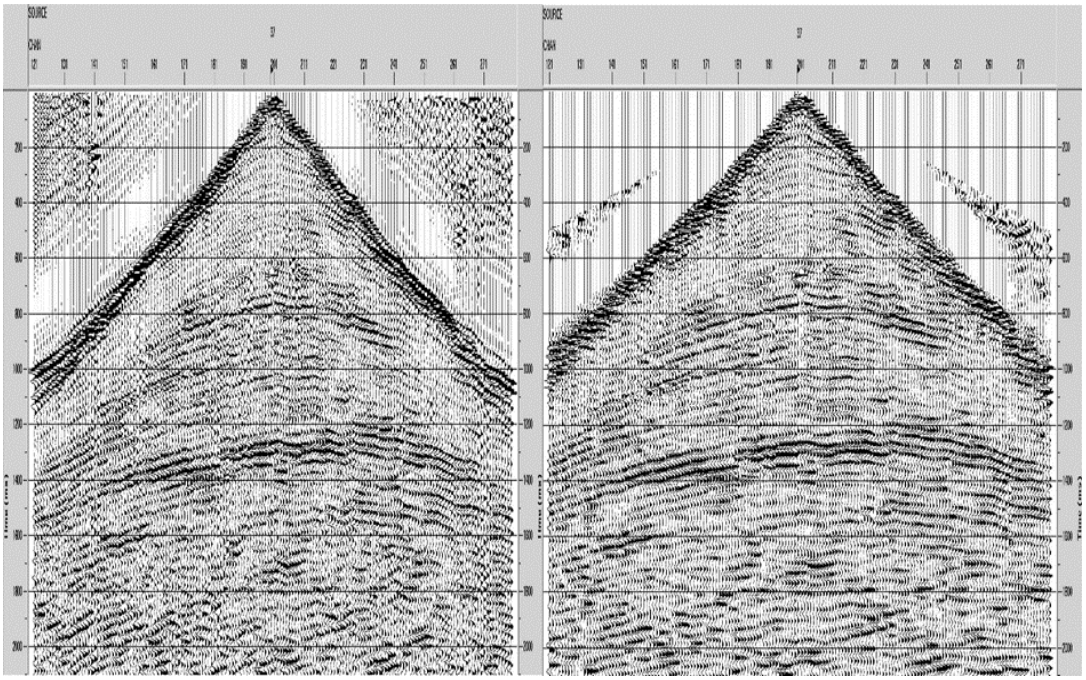

Figure 2.8 Comparison between ground-roll filtering using an Ormsby filter (left panel) and radial transform filtered shot (right panel) shot gather filter

2.4 Velocity Analysis

Following the statics calculations, I switched back to ProMAX software to apply the derived static corrections. These corrections are necessary in order to prepare the data for the stacking velocity analysis. To begin the velocity analysis, I built CMP supergathers (groups of CMP gathers) to increase the number of traces at each analysis point and to ensure accurate velocity picks. To define the supergathers, I combined each 5 CMPs into one display, with an interval of fifteen CMP through the entire line.

Figure 2.9 shows a sample screen-shot for CMP 725 of interactive stacking-velocity analysis in ProMAX. The plot on the left shows the waveform semblance in which I picked the stacking velocities.

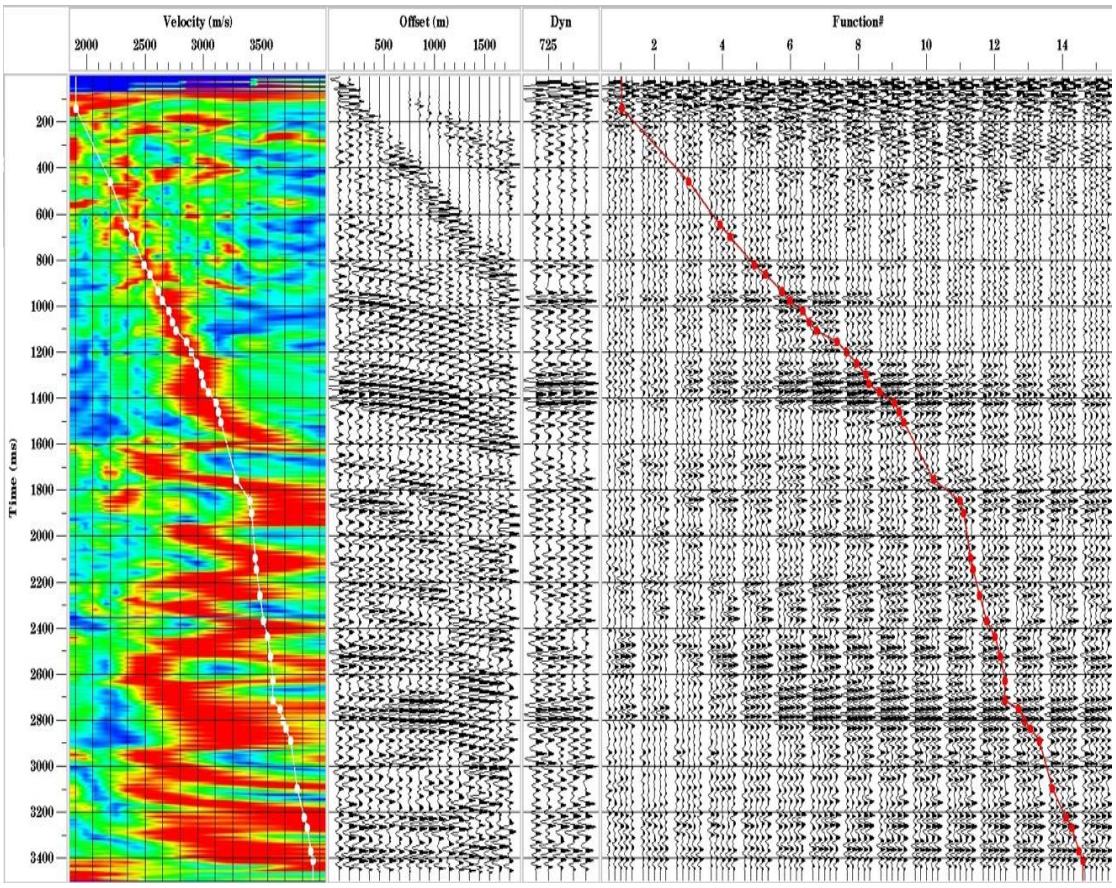

Figure 2.9 Velocity analysis panel for one supergather.

In these displays, velocity picks are made by following the highest semblance (white line on the left-hand side of Figure 2.9) and matching them to the corresponding reflectors on the trace-gather screen (plot in the middle of Figure 2.9). The velocity picks usually have a trend of increasing with depth. The white dots represent the picks, and each pick is matching a reflector

interface with velocity contrast. The panel on the right in Figure 2.9 shows velocity functions (partial stacks of the records). These functions also help in identifying the correct stacking velocity (red line on the right-hand side of the panel).

The picked stacking-velocity profiles at each supergather location were further smoothed and interpolated into a continuous 2-D velocity field and used for Normal Moveout (NMO) corrections. NMO is the difference between the two-way time at a given offset and the two-way time at normal incidence (zero offset for a horizontal reflector). Figure 2.10 shows how the reflections in five CMP gathers (left in the Figure 2.10a) were aligned by the NMO correction (Figure 2.10b). Thus, NMO corrections align the reflections well and allow their stacking in order to produce the final image.

The alignment of reflections in Figure 2.10b depends on the residual statics and dip moveout (DMO) corrections, described below. I therefore repeated the velocity analysis, NMO, DMO, and residual statics three times in order to improve the above picking of stacking velocities. Because of lateral velocity variations and reflector dips, reflections in a CMP gather are not always perfectly aligned after NMO correction. In addition, near-surface velocity heterogeneity can cause additional statics or time delay problems not corrected for by the refraction statics (section 2.2). To reduce such variations, I use residual static corrections, which are time shifts applied to traces in order to correct for arbitrary time delays

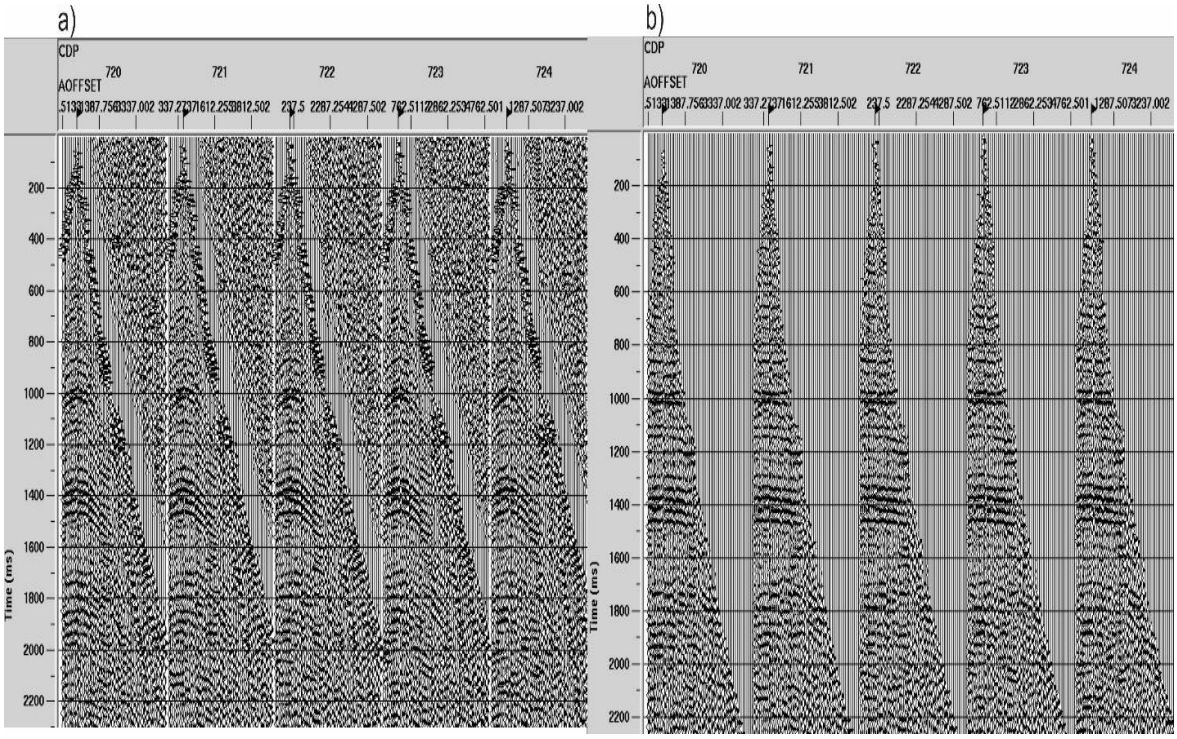

Figure 2.10 CMP gather before (a), and after the applying NMO correction (b).

In ProMAX, I calculated the residual statics by using the correlation autostatics algorithm. Correlation autostatics measures the time shifts relative to a model trace and uses a modified Gauss-Seidel method to partition these time shifts into source and receiver statics (Yilmaz., 2001). The result in Figure 2.11 shows the time shifts for the source in the seismic line. The inverted residual time shifts vary from -18 ms to 80 ms, and the variation of time shift has a trend similar to the topography, as shown in Figure 2.11

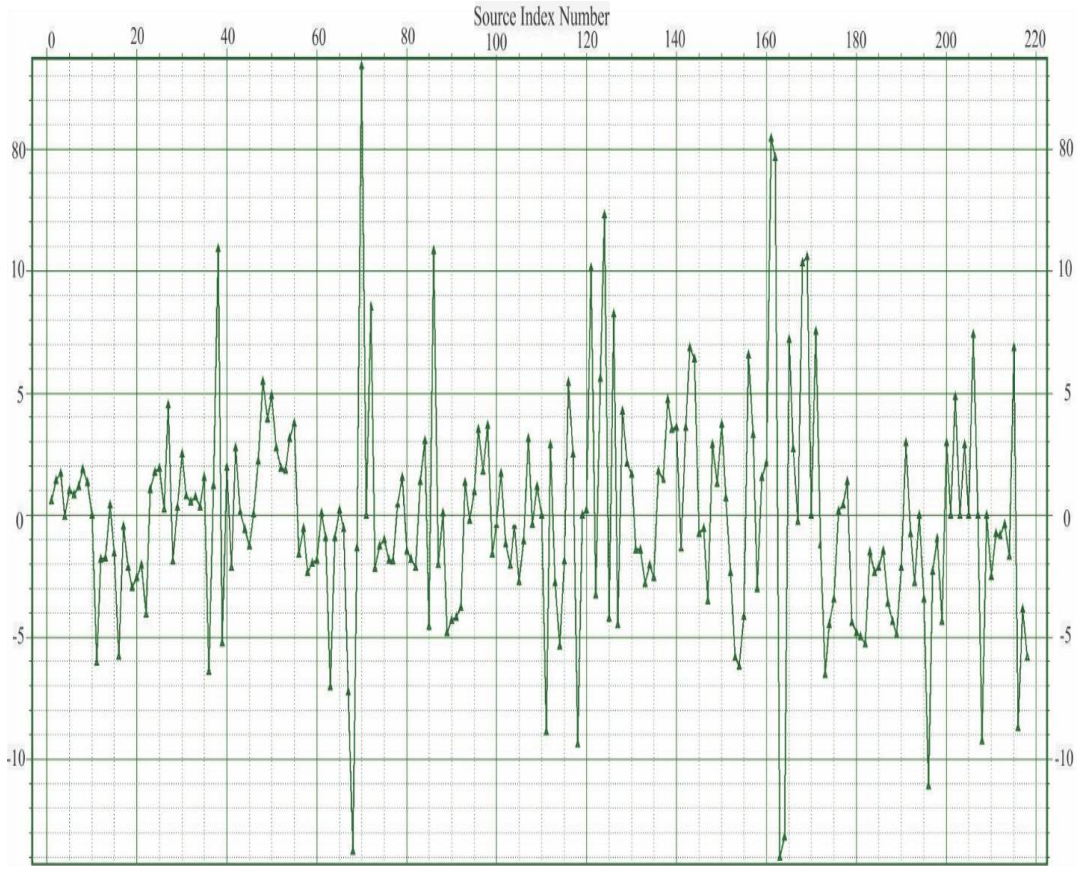

Figure 2.11 Residual statics of the sources, calculated by maximizing the power of the stack in each CMP gather

Figure 2.12 shows the correlation autostatics results calculated for receivers. The time shifts for receivers generally vary from –30 to 25 ms and tend to increase toward the Eastern end of the seismic line. This increasing trend may also be due to the rough topography on the east side of the survey area.

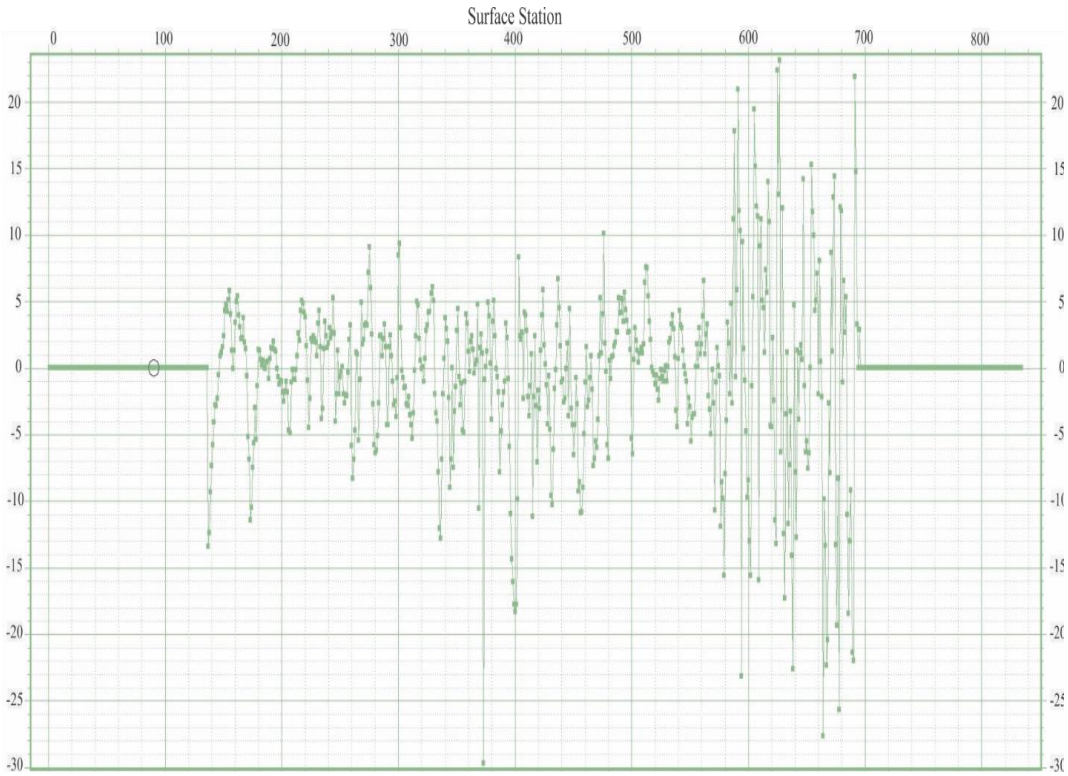

Figure 2.12 Residual statics for receivers, calculated by maximizing the CMP stacked power in each CMP gather

2.5 Stacked Section

After completing the iterative velocity analysis and evaluations of residual statics, the final 2-D stacked section was obtained by stacking the traces within each CMP gather in the dataset (Figure 2.13). In order to enhance the signal and attenuate random noise in this image I also applied a F-X deconvolution filter in ProMAX. The F-X (frequency-spatial) deconvolution operation includes transforming the data in each trace from time to frequency domain, and then applying a complex-valued Wiener prediction filter with respect to the distance at each frequency. This “predictable” signal in distance includes near-constant values (which represents

horizontally aligned reflections) plus any type of periodic signal, corresponding to linear reflections at any arbitrary dips. After the predictive deconvolution, the inverse Fourier transform is used to transform the records back into the time domain. As a result, linear reflections with arbitrary dips become enhanced in the output section, and the random noise is reduced. Some key parameters of the F-X deconvolution are the time window length and the F-X filter start and end frequencies. The time window length is the time gate window of the prediction window. This time should be below 300 ms in case of conflicting dips and event curvature. The F-X start frequency is the minimum frequency of any signal or noise in the dataset in this case I set it as 6 Hz, and the F-X end frequency is the maximum frequency of any signal or noise in the dataset (160 Hz) and higher frequency will be attenuated The resulting stacked section (Figure 2.13) shows clear dipping reflections between 400 to 2000 ms, particularly between CMPs 700 and 1400. Some deeper reflections are seen to about 2800 ms near the beginning of the profile (Figure 2.13). Unfortunately, there is a strong gap between about CMPs 1100 and 1200, which could not be corrected by data processing. This gap is likely caused by poor near-surface conditions: large statics (Figure 4.5), high attenuation, likely poorer source conditions, and strong surface waves. These effects could be due to recording over the very soft sedimentary rocks of the Loess Plateau in China. Similar problems occur in the area of high topography near the end of the profile (CMPs exceeding 1460). In this area, the CMP fold is also reduced (Figure 2.1), which may also affect the quality of imaging. Nevertheless, keeping in mind these difficulties, this section is covering a significant range of reflection times and distances, and it is suitable for application of attenuation-compensation techniques in Chapter 4.

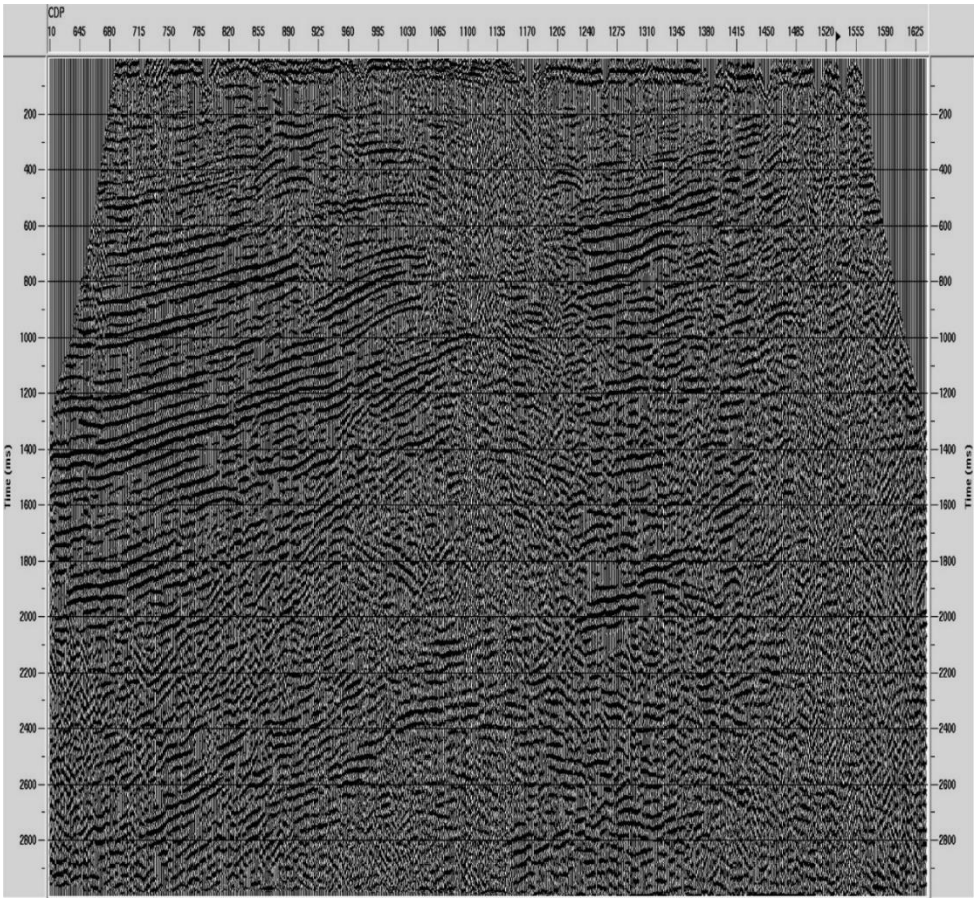

Figure 2.13 Final stacked seismic section.

CHAPTER 3

METHODOLOGY OF INVERSE ATTENUATION FILTERING

The inverse attenuation-filtering procedure used in this Thesis consists of two principal operations: 1) forward modeling of the propagating waveform, followed by 2) inverse filtering in order to remove the effects of attenuation. As mentioned in Chapter 1, a propagating waveform through the Earth subsurface experiences transformations in the form of amplitude reduction and waveform (phase) distortions. In forward modeling, our effort is to accurately model the source waveform as it propagates through the medium taking into account the various factors which lead to wave attenuation. The forward modeling process aims at a true modeling of these physical mechanisms and considering *Q*-type of overall attenuation.

This Chapter and Chapter 4 are based on my contributions to the following published paper:

- *Morozov, I., Haiba, M., and Deng, W., 2018, Inverse attenuation filtering: Geophysics, 83, no. 2, p. V135–V147.*

3.1 Principles of Inverse Attenuation Filtering

Inverse attenuation-filtering is a general approach to remove attenuation effects from seismic records. In contrast to inverse *Q* filtering (Wang, 2008) this method does not start by assuming a *Q* factor existing within the subsurface but rather considers the various physical mechanisms at work. As outlined in Chapter 1, the apparent *Q* factors representing different amplitude-decay and phase-distortion patterns (Figure 3.2) caused by combinations of physical factors. As will be shown in section 3.2, these different physical factors produce different values and frequency dependencies of *Q*. However, combinations of physical mechanisms may not lead to simple combinations of *Q*-factors (Morozov and Ahmadi, 2015). For example, Deng and Morozov (2017) showed that an almost arbitrary frequency-dependence can arise in *Q* for reflection seismic data produced by only elastic layering, without any intrinsic dissipation. Therefore, the first principle of inverse attenuation filtering consists in modeling the attenuation effects directly, by using the specific physical mechanisms (if known) (Morozov et al., 2017). In this Thesis, I consider three of such mechanisms:

1) Wavefront focusing/defocusing (geometric spreading). This is the most common, first-order, frequency-independent effect on seismic waves;
2) Solid viscosity. This is a physical attenuation mechanism common in fluids, and as we argue (Morozov et al., 2018), it should also be common in solid, particularly layered and porous rock.

3) "Phenomenological *Q*", which can be used to describe poorly-known mechanisms, such as scattering. This phenomenological "mechanism" is not truly physical, but it is necessary for comparisons with the conventional inverse-*Q* filtering.

The second principle of inverse attenuation filtering consists in a substantial generalization of the inverse-*Q* filtering (Morozov et al., 2018). Instead of only a single algorithm for correcting the signal spectra for the effects of *Q* (such as Wang, 2008), the modeled propagating source waveform by using any of the mechanisms 1), 2) or 3) above is deconvolved from the seismic record by using several time-variant deconvolution methods. This separation of the procedure into independent modeling and inversion steps leads to improved flexibility and physical accuracy of the approach (described in this Chapter), and to improved deconvolution and imaging results (discussed in Chapter 4).

3.2 Implementation of the Algorithm

When implementing the inverse-attenuation filtering we aimed at allowing various types of input data (prestack or stacked), multiple modeling approaches, velocity and attenuation/dispersion models, and multiple deconvolution methods selectable by the user (Morozov et al, 2018). Such flexibility was possible because of the modular structure of IGeoS processing system (Morozov, 2008), In this system, seismic data processing is described by processing "job" script illustrated in Appendix A. Loading the data, velocity, attenuation, and other models is performed by several IGeoS tools, and all *A*-compensation operations are

combined into the tool named ‘acomp’ (highlighted in Appendix A). Figure 3.1 shows a flowchart implemented by this tool showing its procedures and the key options available

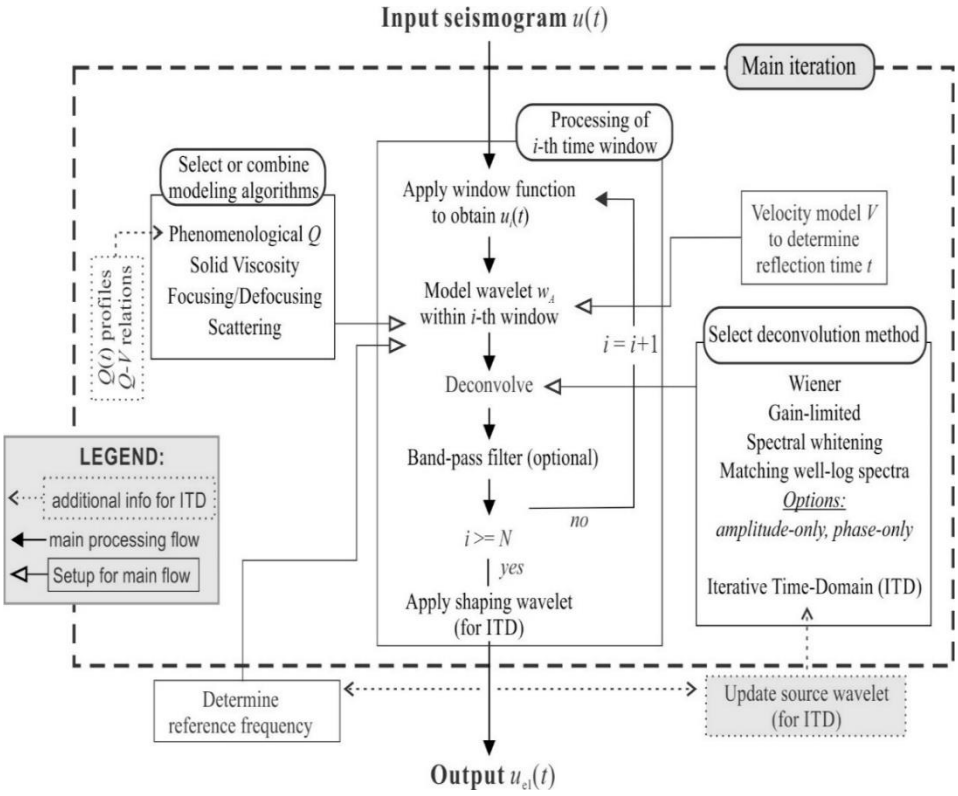

Figure 3.1 Flowchart of Inverse-attenuation filtering

3.3 Attenuation Phenomena

To illustrate the phenomenon of seismic attenuation, Figure 3.2 shows its effect on a propagating waveform for several values of Q. The effects of attenuation are an exponential reduction in the amplitude and a change or distortion of the wave shape. Figure 3.2a shows a harmonic sinusoidal wave propagating in a non-attenuating medium ($Q = \infty$), and we can observe that the shape and the amplitude of the wave is the same through the travel time. Figure

3.2 b shows the same wave propagating through an attenuated medium. Generally, both the logarithmic-amplitude reduction and the phase delays are inversely proportional to *Q*.

As shown in Figure 3.2, velocity dispersion effects (distortion of waveforms) are easily noted in the case of $Q = 5$ within the medium. The low value of *Q* indicates a highly attenuating medium which significantly changes the phase of the waveforms.

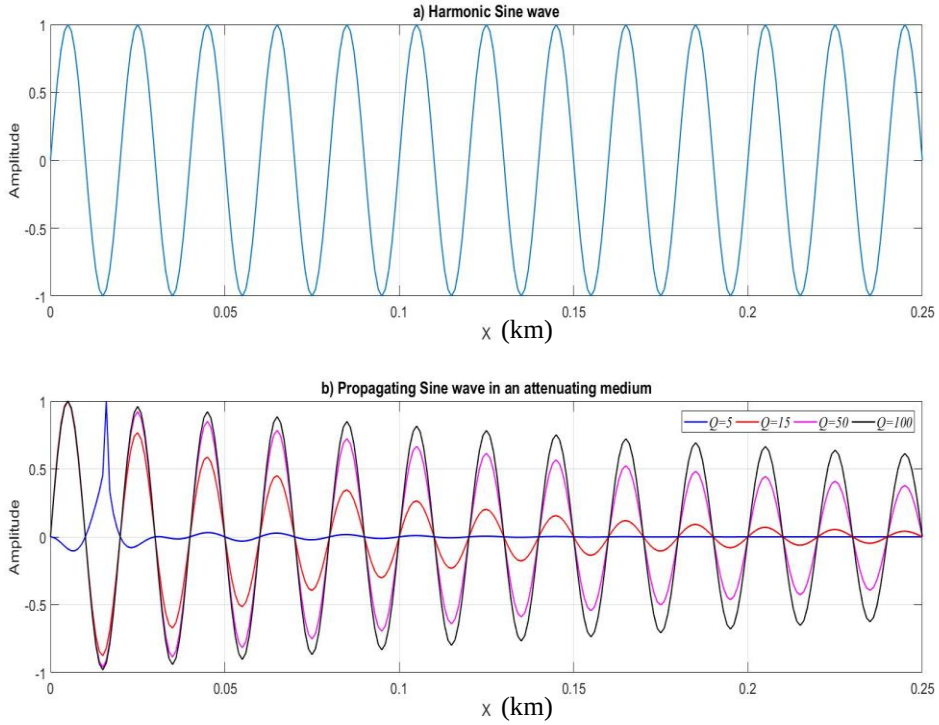

Figure 3.2 Effects of attenuation on seismic waveforms: a) a harmonic sinusoidal wave propagating in a non- attenuating medium, b) the same wave in an attenuating medium with four different $Q = 5$ (blue line), $Q = 25$ (red), $Q = 50$, and $Q = 100$ (black). The frequency of the source is 65 Hz in all examples.

In general, seismic attenuation of a propagating waveform can manifests as amplitude loss, while velocity dispersion effects may or may not be observed, depending on physical mechanism at work. Dispersion effects can be caused due to elastic mechanisms such as focusing

and defocusing, scattering and geometrical spreading. Inelastic mechanisms include grain boundary sliding, large scale intrinsic friction, and small scale defects migration (Yao, 2013).

Geometrical spreading is a frequency-independent attenuation. It depends on the wavefront and its propagating path or angels or spreading, which cause wave focusing and defocusing. Also, frequency-independent scattering is phenomenologically equivalent to geometrical spreading, and it as non-dispersive.

Seismic wave dispersion changes the velocity of the propagating waveforms with changing in the frequency. Velocity dispersion leads to wavelet shape distortion and this causes a difference between the velocities measured in sonic logs compared to the actual velocities in seismic data (Stewart et al., 1984).

Studies have shown that various factor influence velocity dispersion, such as porosity, fractures, and fluid mobility. In some cases, effects of velocity dispersion is neglected due to the difficulties of measuring the velocity dispersion over the seismic frequency band (Sun et al., 2009). As mentioned above, the inverse *Q* filtering methods are limited because of the assumption that velocity dispersion model can be inferred from *Q*. Changing in velocity with frequency (velocity dispersion $V_{(\omega)}$) is usually assumed from $Q^{-1}(\omega)$ by causality relations (Kramers-Krönig, or K-K), which state that $V_{(\omega)}$ is always positive and proportional to $Q^{-1}(\omega)$. However, the K-K relation is constructed over an infinite frequency band extending well-beyond the seismic range of interest (Futterman, 1962). In inverse attenuation-filtering, we restrict ourselves to causal relations built on frequencies within or near the seismic frequency band.

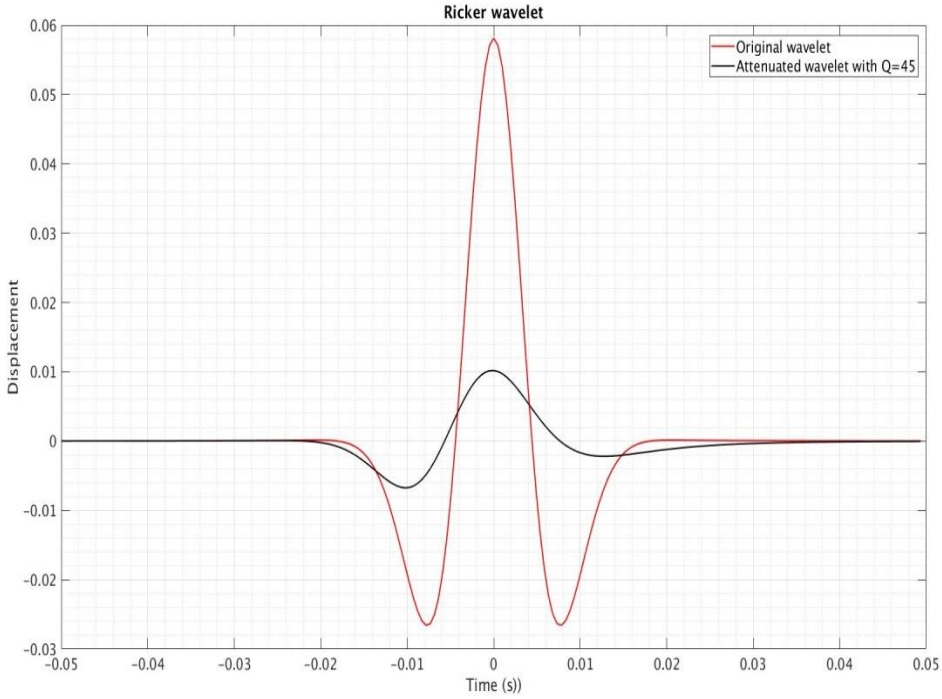

Figure 3.3 Attenuating Ricker wavelet. The red line shows a Ricker wavelet propagating for 1 s in non-attenuated medium, and the black line show the same Ricker wavelet propagating in a medium with Q=45.

Figure 3.3 shows Ricker wavelet propagating in a non-attenuating medium (red) and in a medium (black) with Q = 45. It is clearly shown how the amplitude dropped and the shape of the same wavelet changed when propagating in an attenuating medium.

Figure 3.4 illustrates the attenuation effects on the amplitude spectrum and the wavelet phase shape. The frequency peak of the original wavelet is shifted to lower frequency after propagating in an attenuated medium and it lost more than half of its amplitude (black line Figure 3.4 a). The original wavelet was zero phase (red line Figure 3.4 b) and after the

propagation the phase is changed (black line Figure 3.4 b) illustrates the attenuation effects on the signal spectra.

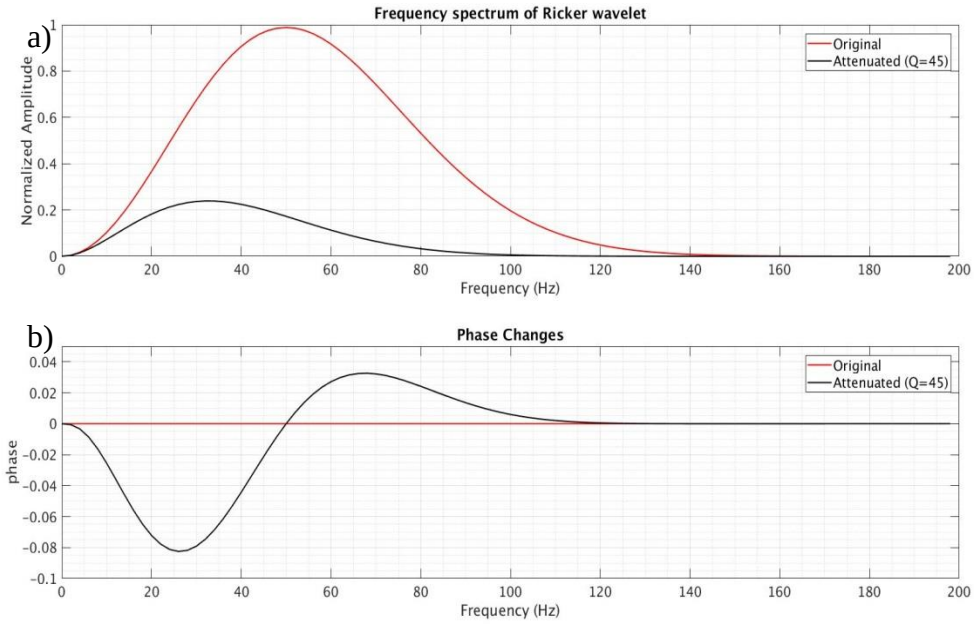

Figure 3.4 a) shows the frequency spectra corresponding to the wavelets in Figure 3.3. and Figure 3.4 b) is the phase changes of the attenuated Ricker wavelet comparing with the original Ricker wavelet phase

When we correct for attenuation and waveform distortions due to velocity dispersion, we broaden the spectra and increase the resolution of seismic data. There exist several approaches to remove the attenuation effects from the seismic records such as the conventional inverse *Q* filtering. However, those approaches have some limitations due to their dependence on two assumptions: firstly, the viscoelastic-*Q* model for attenuation, and secondly, in their use of the K-K relations to calculate velocity dispersion assuming that it can be inferred from the *Q*. Both assumptions are inaccurate, as can be seen, for example, from the fact that pore-fluid related

attenuation involves two types of P waves (fast and slow) which cannot be accurately described by a single P-wave *Q*-factor (Morozov and Deng, 2016).

In the study by Morozov et al. (2018), we remove these limiting assumptions and propose a general approach of inverse attenuation-filtering. In inverse attenuation filtering, *Q* factor is considered as an apparent attribute of waveforms traveling through a medium which expands the attenuation filtering proposed in this Thesis.

Inverse attenuation-filtering method has the advantage to imply the apparent characters of *Q* and *V* to formulate general approach for attenuation corrections due to the effects of the apparent *Q* and *V* on the waveforms. Attenuation correction requires forward modeling of the attenuation effects and inverse filtering of these effects. Generally, these effects can be approximated by linear filters with parameters slowly varying with time. In this manner, the forward modeling and the inverse filtering can be performed separately and then combined in a simple time-windowing procedure.

The attenuation of a propagating wave due to any effect may be described in terms of α and Δk, or equivalently by parameters $Q^{-1}(\omega)$ (attenuation) and $V^{-1}(\omega)$ (phase slowness), at each point along its path. It is convenient to combine these parameters in the complex-valued slowness parameter:

$$s^*(\omega) \equiv s(\omega) + is'(\omega) \equiv V^{-1}(\omega)\left[1 + \frac{1}{2}Q^{-1}(\omega)\right]. \tag{3.1}$$

In *Q*-filtering literature, it is often stated that "the dispersion is a result of requirement that the wave propagation in an absorbing medium must be *causal*" (Hargreaves and Calvert,

1991). It is also often inferred from the K-K relations that $dV/d\omega$ is positive within the seismic band (e.g., Wang, 2008). Nevertheless, causality still does not imply that the dispersion is due to attenuation nor that it must have a definite sign. The K-K relations consist of slowly-converging integrals (Aki and Richards, 2002), and definitive relations between $Q^{-1}(\omega)$ and $V^{-1}(\omega)$ can only be found for certain forms of these functions defined across infinite frequency bands (Futterman, 1962; Aki and Richards, 2002; Wang, 2008). Within the narrow exploration-seismic frequency band, the K-K relations do not dictate any particular relation between of Q^{-1} and $dV/d\omega$.

In practice, the K-K relations represent a fairly weak constraint only expressing the causality of the wave-propagation process. In the time domain, causality simply means that at any travel distance x, the amplitude of the wave equals zero at all times preceding some "wave onset:" $t < t_{onset} = xV_0^{-1}$, where V_0 is some velocity. In Futterman's (1962) model, V_0 equals $V(\omega_0)$ at an extremely low cutoff frequency ω_0. In several other models (Azimi, 1968, or linear solids), V_0 is the phase velocity at infinite frequency (denoted V_∞), and in the constant-Q and power-law models (Kjartansson, 1979; Műller, 1983), $V_0 = \infty$. Intuitively, it seems clear that such a basic assumptions ought not constrain the relation between $Q^{-1}(\omega)$ and $V^{-1}(\omega)$ at any given frequency. In the frequency domain, the identity $w(t < t_{onset}) \equiv 0$ yields a reciprocal integral relation between the real and imaginary parts of phase slowness in equation (1.3) (Aki and Richards, 2002):

$$s(\omega) = V_0^{-1} + \mathrm{H}\left[s'(\omega)\right], \text{and } s'(\omega) = \frac{\alpha_0}{\omega}\mathrm{H}\left[s(\omega) - V_0^{-1}\right], \tag{3.2}$$

where H is the Hilbert transform, and α_0 is another arbitrary constant of dimensionality

[1/distance].

To illustrate the causality constraints in the frequency domain, Figure 3.5 shows a hypothetical attenuation spectrum $s'(\omega)$ with a trough and a peak and the corresponding phase-delay spectrum $s(\omega)$ evaluated by equation (3.2). The complex slowness $s+is'$ is transformed into an inverse Q factor and phase velocity by using relations $Q^{-1}=2s'/s$ and $V=s^{-1}$.

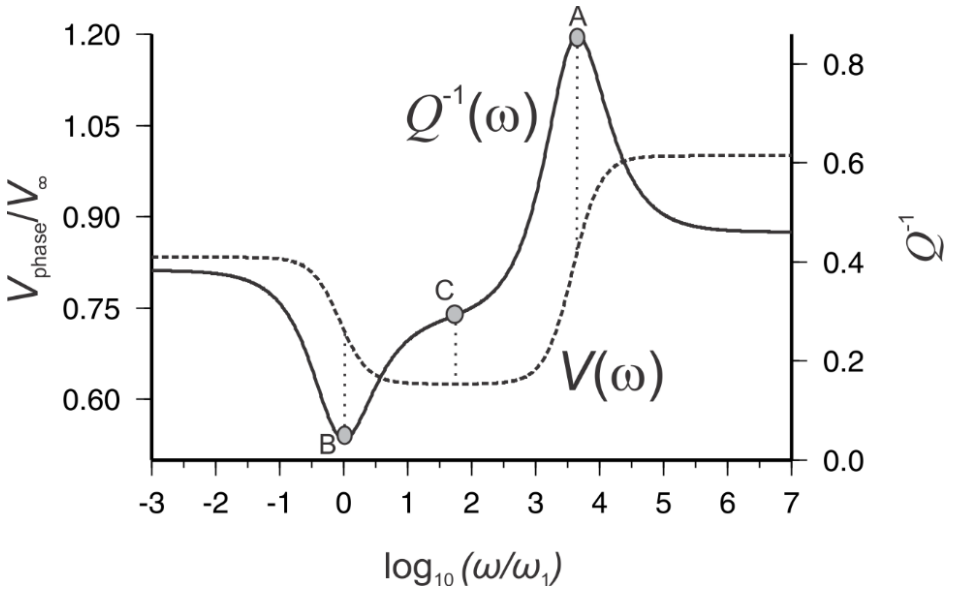

Figure 3.5 Relations between frequency-dependent inverse Q-factor (solid line) and phase-velocity dispersion (dashed line) for a simple waveform with one through and one peak

Assuming our measurements take place within a relatively narrow frequency band, three characteristic regimes can be recognized (labels A, B, C in Figure 3.5). If the observation band is located near the attenuation peak (regime A in Figure 3.5Figure 3.3) or trough (regime B), a near-constant Q would be observed, and velocity dispersion is positive or negative, respectively. The rate of dispersion $dV/d\omega$ is not proportional to Q^{-1} as in Futterman's and other common

models (Wang, 2008). Instead, the $dV/d\omega$ is related to the variation in Q^{-1} at these much lower and much larger frequencies (Figure 3.5). If the observations happen to be made between the peak and trough of Q^{-1}, the dispersion is near zero (regime C in Figure 3.5).

Models commonly used in inverse Q filtering (e.g., Futterman, 1962) imply a sole peak in $Q^{-1}(\omega)$ (regime A in Figure 3.5), despite the fact that this is often not the case in practice. While variations of Q are difficult to measure within the seismic band, asymptotes of $Q^{-1}(\omega)$ at $\omega \to 0$ and $\omega \to \infty$ are totally unknown. Consequently, regimes A to C can be difficult to identify. In a given measurement, we can expect arbitrary velocity dispersion $dV/d\omega$ alongside a (relatively) arbitrary frequency-dependence of Q. These dependences can be approximated by linear functions of $\log \omega$:

$$s'(\omega) = \frac{1}{V_r}\left(1 + s_1 \log\frac{\omega}{\omega_r}\right), \text{ and } s'(\omega) = \frac{1}{2V_r Q_r}\left(1 + s_1' \log\frac{\omega}{\omega_r}\right), \tag{3.3}$$

where ω_r is some reference frequency, and s_1 and s_1' are dimensionless parameters characterizing the velocity dispersion and frequency-dependence of Q for the wave. Parameterization in terms of $\log\omega$ is chosen to resemble Futterman's (1962) dispersion relation and similar equations. For measurements at the top of a dissipation peak (regime A in Figure 3.5), s_1 takes on the smallest value of $s_1 \approx -1/(\pi Q_r)$ (Futterman, 1962). With this parameterization, group slowness differs from the phase one by a constant:

$$U^{-1}(\omega) = \frac{d(\omega s)}{d\omega} = s(\omega) + \frac{s_1}{V_r}, \tag{3.4}$$

and the frequency dependence of $q \equiv Q^{-1}$:

$$q(\omega) = \frac{1}{Q_r} \frac{1 + s_1' \log \dfrac{\omega}{\omega_r}}{1 + s_1 \log \dfrac{\omega}{\omega_r}} \approx \frac{1}{Q_r}. \tag{3.5}$$

Although s_1' is difficult to measure, equation (3.4) shows that both s_1' and s_1 are equally important for the effect of attenuation. Figure 3.4 shows the relations given by equations (3.3) with compared to several standard dispersion laws and a solid-viscosity relation.

3.4 Time-Variant Modeling and Deconvolution

Time-variant filtering is an efficient and convenient method for attenuation compensation, spectral whitening, time-spectral analysis, and other reflection seismic processing applications. Time-variant filtering is a convolutional operators which depends on Fourier transform variables to shape the spectrum of a time series (Margrave, 1998).

In a linear time-variant system, the relation between the output $u_2(t)$ and the input $u_1(t)$ is presented by

$$u_2(t) = \int_{-\infty}^{\infty} f(t,t')u_1(t')dt', \tag{3.6}$$

where $f(t,t')$ is the response measured at time t to an delta-function impulse at time at time t'

This function is nonzero only for $t \approx t'$ (within wavelet length), where it approximately depends only on the time difference: $f(t,t') \approx f_0(t-t')$. Therefore, within a vicinity of a point within the seismic record, the time-variant transformation (3.6) approximately represents ordinary convolution: $u_2(t) \approx \int_{-\infty}^{\infty} f_0(t-t')u_1(t')dt'$. This approximation is used in the time-variant filtering included in IGeoS tool 'acomp'.

To implement time-variant modeling and deconvolution in tool 'acomp', I apply a series of overlapping Hanning taper functions $\phi_n(t)$ to each seismic record. Each taper element consists of a flat portion centered on time t with two cosine-shaped ramps of durations Δt, which is estimated by scaling the duration of the source wavelet T_w. The intervals between time tapers, are selected equal the same Δt, so that a sum of all tapered records produces the untampered one (Morozov et al., 2018). Within each window, the time-variant filtering is implemented by convolution or ordinary frequency-domain filtering, and the resulting records are summed to achieve an attenuation-filtered signal:

$$u_{el}(t) = \sum_n F_n * \left[\phi_n(t)u(t)\right]. \qquad (3.7)$$

The windowing functions are shown in Figure 3.6 and normalized by the condition $\sum_n \phi_n(t) \equiv 1$ at any time t, so that the input signal is unchanged $\left(u_{el}(t) \equiv u(t)\right)$ when no filters F_n are applied. Two general types of filters F_n in eq. (3.7) are used in subsequent processing. First, to implement forward modeling of seismic wavelets, filters representing physical or Q-type

effects of attenuation are used. These filters implement the time-variant "attenuation operators" $\hat{\mathrm{A}}(t)$, which transforms the source waveform at time t that would have been measured within a perfectly elastic subsurface (denoted $w_{\mathrm{el}}(t)$) into the actual attenuated wavelet $w(t)$. $w = \hat{\mathrm{A}} w_{el}$.

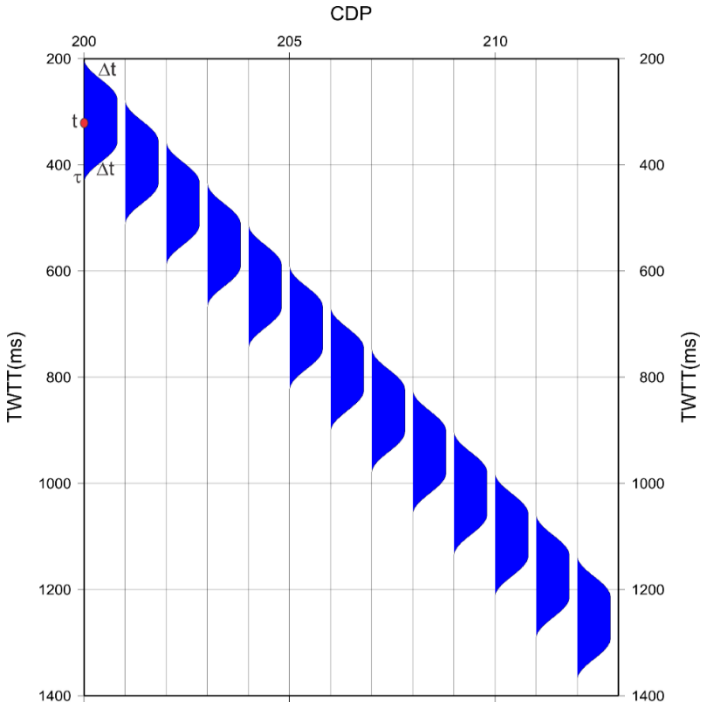

Figure 3.6 Overlapping Hanning-tapered time windows $\phi_n(t)$ used for modeling the propagating waveform and deconvolution procedures. Times t Δt, and τ are indicated.

Three forms of such operators are described in subsection 3.3. Second, in order to perform A-compensation, inverse attenuation operators $F_n(t) = \hat{\mathrm{A}}^{-1}(t)$ are used. Because attenuation reduces the high-frequency energy of the wavelet and can bring it below the noise level, evaluation of the operators at large times t requires careful regularization, as described by Wang (2008). In data applications in Chapter 4, I compare the well-known frequency-domain

approach to such regularization called Wiener deconvolution (Morozov et al., 2018) and a novel iterative time-domain deconvolution (ITD) technique. The ITD approach is described in subsection 3.6.

3.5 Modeling of Attenuation Effects

In this section, I describe three key physical effects leading to seismic wave attenuation. These physical effects or their combinations can be used for constructing the attenuation operator in IGeoS tool ‘acomp’ which is further utilized for compensation of the attenuation effects. Measuring and modeling the attenuation effects requires good knowledge of rock-physics mechanisms of internal friction which is not well known and sometimes controversial subject. However, attenuation effects can always be modelled by composing an appropriate time-dependent attenuation operator.

Modeling of attenuation accumulated along a propagation path is a complex task. In current attenuation-modeling methods, there are two general approaches to forward modeling of seismic waves in spatially-heterogeneous an elastic media frequency-domain and time-domain. In frequency-domain methods (for example, (Štekl and Pratt (1998)), forward modeling is implemented by wave equations utilizing complex-valued and frequency-dependent viscoelastic moduli. This method is suitable and advantageous for full waveform inversion when only a limited number of frequencies are needed. By contrast, in order to reproduce the variation of a seismic waveform with time, time-domain finite-difference methods can be used. In these

methods, the attenuated wavefield is calculated by time stepping the differential equations over the time-dependent viscoelastic moduli (Blanch et al., 1995).

Generally, in the above and other waveform modeling approaches, and also in inverse-*Q* filtering methods, the *Q* factor is considered to be the key physical property of the medium. However, the physical character of the *Q* is actually quite a complicated problem. Since *Q* is defined as a property of propagating seismic waves or oscillations compared to an elastic case (Chapter 1) but no "elastic" equivalent of the Earth is available, the *Q* cannot be measured directly by any other physical experiment. Furthermore, because *Q* can only be measured from seismic waveforms of sufficient lengths, it cannot be rigorously attributed to an individual point within the subsurface. For example, White (1992) showed that in order to measure a Q =100 with 30% accuracy in vertical seismic profile (VSP) records, a roughly 100-ms waveform is needed. Morozov and Ahmadi (2015) argued that the *Q* factor is only a mathematical hypothesis ("apparent" property) and, as such, it is unclear how accurately it can be used to describe the heterogeneous Earth. However, Morozov et al. (2018) argued that for attenuation compensation in seismic records, the apparent character of *Q* is sufficient, and it does not need to be property of the medium. Thus, if the subsurface structure is known, the effects of multiple physical mechanisms on the propagating waveform can be modeled, giving the apparent *Q* and dispersion effects. Only these quantities are needed for attenuation corrections.

In the *A*-compensation approach (Morozov et al., 2018), the attenuation and dispersion corrections at time *t* are obtained by comparing the "elastic" and "inelastic" waveforms at time *t*.

For a plane wave propagating through an elastic homogenous medium, the waveform at time *t* can be described as:

$$w_{el}(x,t) = A_0 \exp(-i\omega t + ik_0 x), \tag{3.8}$$

where *x* is the coordinate (depth in this case), k_0 is the wavenumber, and A_0 is the amplitude. The same plane wave traveling through an inelastic medium it can be described as:

$$w(x,t) = A\exp(-i\omega t + ikx - \alpha x) = A\exp(-i\omega t + ik^* x), \tag{3.9}$$

where $k^* = k + i\alpha$ is the complex-valued wavenumber. Due to attenuation effects, the amplitude changes from A_0 to *A* and the wave number changes from k_0 to $k=k_0+\Delta$. The new parameter α in equation (3.9) is the frequency-dependent spatial attenuation coefficient, which can be estimated from the logarithmic spatial decrement of the amplitude. The transformation from the elastic case $w_{el}(x,t)$ to the inelastic case $w(x,t)$ can be described by a linear operator $\hat{A}$, as $w = \hat{A}\, w_{el}$. In the limit of zero frequency, there should be no attenuation, and *A* is simply A_0 (Morozov et al., 2018). Consequently, w_{el} represent an eigenvector of operator $\hat{A}$:

$$\hat{A} w_{el} = \zeta w_{el}, \tag{3.10}$$

where the eigenvalue equal:

$$\zeta(x) \equiv \exp(i\Delta k x - \alpha x). \tag{3.11}$$

From the modified k and A, the phase velocity and Q can be obtained as: $V \equiv \omega / (k_0 + \Delta k)$ and $Q^0 (k_0 + \Delta k) / 2\alpha$. The quantities k, V, α and Q define the amplitude decay of the propagating waveform through a medium (Morozov and Ahmadi, 2015).

In application to an "elastic" seismic waveform w_{el}, the attenuation operator $\hat{A}$ represents a filter applied by using the convolution operation. This operator also consists of various attenuation mechanisms such as geometric spreading, solid viscosity, scattering and the traditional Q-type (viscoelastic) attenuation. This combination of different physical factors can be represented by a convolution of filters corresponding to each of these factors:

$$\hat{A} = \hat{A}_{Geometric} * \hat{A}_{Scattring} * \hat{A}_{Q} * \hat{A}_{Viscosity}. \quad (3.12)$$

Now let us discuss the effect of the attenuation operator on the reflection seismic waveform. A plane seismic wave reflected from layered Earth can be described by the convolutional model. To illustrate the convolutional model, let us consider a time window centered at some two-way reflection time t, and denote the seismic reflectivity $r(t, \tau)$, where τ is the local time of the waveform selected be $\tau = 0$ at the center of the window. The reflected waveform $u(\tau)$ is a convolution of reflectivity $r(\tau)$ with source signature $S(\tau)$, receiver response $R(\tau)$, and downward and upward propagation-path effects denoted D*A

$$u = S * R * D * A * r. \quad (3.13)$$

In this relation, factor D represent the deterministic effects (such as geometrical spreading or amplitude variations with offset), which are corrected for in seismic reflection data

processing procedure, factor A represents the time-domain attenuation operator equation (3.12) and the source and receiver effects can be combined in a source wavelet, $w_S \equiv S * R$.

To remove the attenuation effects from seismic records, we need to construct an inverse of the modeling operator. The filter would transfer the inelastic case to an elastic one. To correct for attenuation effects, we must remove factor "*A*" in equation (3.13). This is done by applying the inverse attenuation filter $\hat{F}=\hat{A}^{-1}$ which will produce a non-attenuated reflected waveform which would thus be recorded over a theoretical elastic medium:

$$u_{el}(\tau) = F * u = w_S * D * r. \tag{3.14}$$

After modeling the attenuation filter $\widehat{A}$ for the propagating waveform, a deconvolution process is applied to evaluate the filter F above or to directly evaluate the corrected $u_{el}(\tau)$. Multiple deconvolution methods can be applied depending of the properties of datasets and the purpose of the deconvolution process.

3.5.1 Geometric Spreading

Elastic mechanisms are the redistribution of wave energy and without net energy loss. These effects can be divided into geometric spreading, multipathing, wavefront focusing and defocusing, and scattering on layers and small-scale heterogeneities within the medium. Geometric spreading is one of the strongest effects that cause seismic amplitude reduction. It dominates the frequency-independent portion of the waveform attenuation. In conventional *Q*-filtering, geometric spreading effects usually neglected because it is expected to be corrected

prior to applying the inverse-*Q* filtering algorithms. Frequency-independent small-scale scattering is phenomenologically equivalent to variations of geometric spreading (Morozov, 2010), and therefore it is phenomenologically included in geometrical spreading. Multipathing and local focusing/defocusing may similarly represent very complex processes, but frequency-independent parts of their effects on seismic waveforms can be phenomenologically attributed to geometric spreading (Morozov, 2010).

In the convolutional equation (3.12), the empirical geometric-spreading effects above, can be represented by multiplication of several factors describing the various types of possible geometric spreading effects:

$$A_{\text{Geometric}}(t,x,\omega) = G_0 \times \frac{1}{V_{RMS}^{\zeta} t_0} \times \frac{1}{t^{V}} \times \frac{1}{R^{\zeta}} \times \exp(-\delta t) \times \exp\left(- \int\limits_{\text{Ray path}} \gamma dt \right). \qquad (3.15)$$

In IGeoS tool ‘acomp’, combinations of these factors can be selected during data processing, and some of the factors are also available in geometrical-spreading corrections in ProMAX reflection seismic processing software. In eq (3.15), the factor G_0 is a normalization constant selected to ensure $G(t_{ref},0)=1$ at the reference time t_{ref}. factor $\frac{1}{V_{RMS}^{\zeta} t_0}$ is the approximation for the geometric spreading in a layered Earth by Newman (1973). V_{RMS} represent the RMS velocity at two-way normal incident time t_0. The value of the exponent ζ is kept as an arbitrary value for simplicity as in (Newman, 1973) model exponent $\zeta = 2,$ also a value of can be

used in ProMAX. For refractions, additional frequency-dependent factors can also be included in geometric spreading (Yang et al., 2007); however, I do not consider them in this Thesis.

3.5.2 Phenomenological (*Q*-type) Attenuation

In contrast to energy-conserving elastic effects, inelastic effects cause intrinsic attenuation resulting in dispersion and a reduction of wave energy, as described in section. The forward modeling aims at a true modeling of these physical mechanisms and considering *Q*-type of overall attenuation. While there are several approaches to modeling of these effects and their compensation, the most common is the phenomenological attenuation model in which a *Q*-factor is assumed to represent the mechanical friction within the medium.

Different *Q* models have been developed for forward modeling of attenuation effects, such as the constant-*Q* model (Kjartansson, 1979), Klosky's model (Futterman, 1962), and Strik-Azimi's model (Futterman, 1962; Strick, 1967; Azimi et al., 1968). The constant-*Q* model (Kjartansson, 1979) is most commonly used in forward modeling.

Frequency-dependent phenomenological models, $Q(\omega)$, may be used to represent the seismic wave propagating in an inelastic/attenuating medium. In order to satisfy the causality principle, the phase velocity must also be frequency-dependent (Aki and Richards, 2002):

$$\frac{\omega}{V(\omega)} = \frac{\omega}{V_\infty} + \mathrm{H}\left[\frac{\omega}{2V_\infty Q}\right], \tag{3.16}$$

where $\mathrm{H}[\ldots]$ is the Hilbert transform and V_∞ is the wave velocity at the infinite angular frequency. For weak and near-constant attenuation ($Q >> 1$), within the range of frequencies

used in seismic exploration, V should increase with frequency as approximated by Aki and Richards (2002):

$$\frac{V(\omega)}{V(\omega_r)} = 1 + \frac{1}{\pi Q}\log\left(\frac{\omega}{\omega_r}\right), \tag{3.17}$$

where ω_r is an arbitrary reference frequency.

Figure 3.7 shows this relation for different values of the Q. Because of attenuation, the phase velocity also becomes complex-valued (Aki and Richards, 2002), which can be described by introducing a complex-valued slowness $s^* \equiv 1/V^*$:

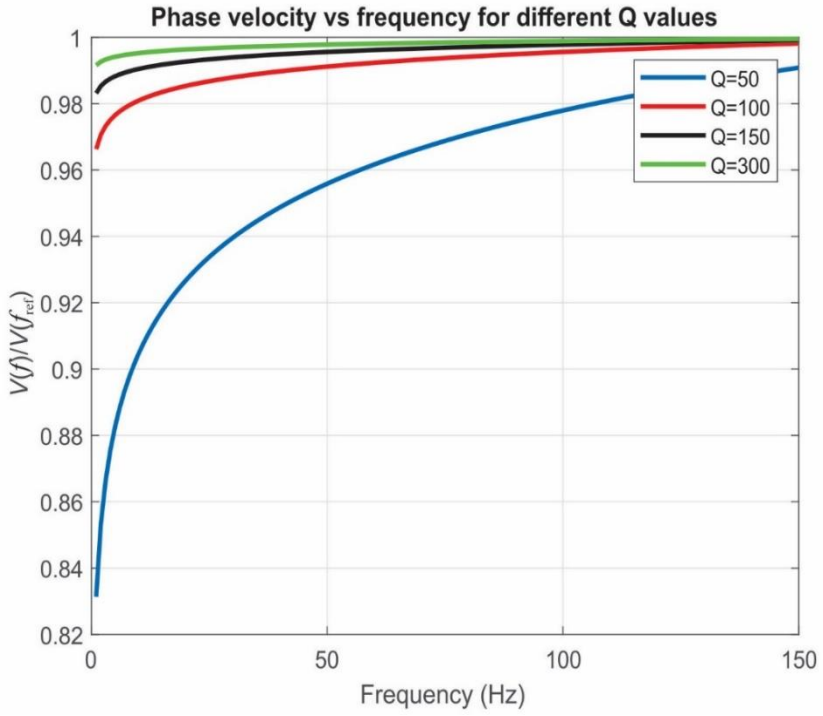

Figure 3.7 Phase velocity vs frequency along with different values of Q. The curves represent velocity dispersion described in equation (3.15). The reference frequency w_{ref} is taken equal 200 Hz.

$$s^*(\omega) \equiv s(\omega) + is'(\omega) \equiv V^{-1}(\omega)\left[1 + \frac{i}{2}Q^{-1}(\omega)\right]. \tag{3.18}$$

In each specific attenuation model, the reference frequency ω_r and reference phase velocity $V(\omega_r)$ and quality factor $Q(\omega_r)$ may be chosen by using different principles. For example, Kjartansson (1979) chose the reference velocity to be the velocity at extremely high frequency, well above the seismic frequency band, whereas Futterman (1962) used an extremely low value of ω_r By contrast, our approach, is to set the reference frequency equal the dominant frequency of the signal and adjust $V(\omega_r)$ and quality factor $Q(\omega_r)$ after each iteration of attenuation corrections (Morozov et al., 2018). This removes from our work any dependence on a fixed velocity relation and on the arbitrary parameter ωr_{ef}

Finally, using our phenomenological *Q*-type attenuation models allows combining multiple forms of $Q(\omega)$in the convolution process equation (3.12). For example, using the 'acomp' tool, we can combine the intrinsic and scattering attenuations by adding their inverse *Q*-factors as:

$$Q^{-1}_{\text{observed}} = Q^{-1}_{\text{intrinsic}} + Q^{-1}_{\text{scattering}}. \tag{3.19}$$

3.5.3 Solid Viscosity

In contrast to the phenomenological *Q* described in subsection 3.3.2, solid viscosity (for rocks) and ordinary viscosity (for fluids) are true properties of the medium. These properties can be rigorously characterized by continuum mechanics without the use of internal degrees of freedom (Morozov and Deng, 2016). To model seismic P-waves traveling through an isotropic

medium of modulus M and solid viscosity η_M the mechanical wave equation is given by Morozov and Deng, (2016):

$$\rho\ddot{u} = Mu'' + \eta_M \dot{u}'', \tag{3.20}$$

where the primes denote the spatial derivatives in the direction of propagation X, and the over dots are the time derivatives.

One of the general solutions of this equation is an exponentially decaying plane wave propagating in the positive X direction is given by equation (3.11), where the complex wavenumber equals:

$$k^*(\omega) = \omega\sqrt{\frac{\rho}{M - i\eta_M\omega}} = \frac{\omega}{V_{el}}\frac{1}{\sqrt{1 - i\dfrac{\omega}{\omega_0}}}, \tag{3.21}$$

the elastic velocity V_{el} is defined by $M = \rho V_{el}^2$, and the characteristic frequency is $\omega_0 = M/\eta$.

The apparent V and Q are defined as $V = 1/\mathrm{Re}\left(1/V^*\right)$ and $Q = \mathrm{Re}\left(1/V^*\right)/\left[2\,\mathrm{Im}\left(1/V^*\right)\right]$, where the complex phase velocity equals $V^* = \omega/k^* = V_{el}\sqrt{1 - i\dfrac{\omega}{\omega_0}}$. From these relations, the V and Q are

$$V(\omega) = \frac{V_{el}}{\mathrm{Re}\left(\sqrt{1 - i\dfrac{\omega}{\omega_0}}^{-1}\right)}, \quad \text{and} \quad Q(\omega) = -\frac{1}{2}\cot\left[\frac{1}{2}\mathrm{Arg}\left(1 - i\frac{\omega}{\omega_0}\right)\right]. \tag{3.22}$$

From the second of these equations, at seismic frequencies, ($\omega \ll \omega_0$) the Q is inversely proportional to frequency: $Q(\omega) \approx \omega_0 / \omega$. This frequency dependence is used for modeling solid viscosity in IGeoS tool 'acomp' (Morozov et al., 2018),

3.6 Iterative Time Domain Deconvolution

Among a broad variety of deconvolution methods that can be used as inverse *A*-compensation filters F_n, in this section, I only describe the promising new, iterative time-domain (ITD) method suggested in our recent paper (Morozov et al., 2018). The advantage of time-domain deconvolution is that it does not require constructing an inverse attenuation operator $\hat{A}^{-1}(t)$ and considering its regularization. Instead, According to the linear convolutional model (section 3.3), the recorded reflected waveform $u(\tau)$ (where τ is the "local" time in the vicinity of reflection time t) is a convolution of $r(\tau)$ with the current source wavelet $w(\tau)$:

$$u = w * r \tag{3.23}$$

If the subsurface is "elastic" (for example, after *A*-compensation is applied), the same relation holds, and it is assumed that the reflectivity is the same (it is always "elastic"): $u_{el} = w_{el} * r$ By considering realistic forms of $r(t)$ such as sequences in which the stronger reflections are sparse, $u(t)$ can be transformed into $u_{el}(t)$ without evaluating the operator $\hat{A}^{-1}(t)$. In addition, $r(t)$ can be constrained by geological or well-log data, for example, by emphasizing

the reflections from horizons identified in well logs. Such constraints increase resolution and allow focusing on the structure of interest.

The ITD method follows the approach broadly used to compute receiver functions in earthquake seismology (Ligorría and Ammon, 1999). In this approach, the time series $r(t)$ is sought in the form of a series of spikes of amplitudes r_i located at times τ_i:

$$r(\tau) = \sum_{i=1}^{N} r_i \delta(\tau - \tau_i), \tag{3.24}$$

where $\delta(\tau)$ is the delta function. The input (attenuated) signal is therefore approximated as

$$u(\tau) = \sum_{i=1}^{N} r_i w(\tau - \tau_i). \tag{3.25}$$

The determination of the values of τ_i and r_i, details of the algorithm, and numerical tests of this method are described by Morozov et al. (2018). Because of the limited bandwidth of the wavelet $w(\tau)$, the times t_i tend to be separated by at least half of the dominant period of the data, and therefore the strongest reflections accounting for most of the energy are "sparse". Equation (3.24) can also be used to form a "skeletonized" image of two-way travel times τ_i offering additional interpretational value (Li et al., 1997).

In the output of the iterative deconvolution equation (3.8), the "skeleton" signal $r(t)$ is often convolved with a zero-phase wavelet $w_s(t)$ of some simple shape and bandwidth close to that of the expected $w_{el}(t)$. Ligorría and Ammon (1999) recommend using a Gaussian wavelet for

this purpose. In IGeoS 'acomp' tool, this wavelet is called the "shaping" wavelet and viewed as an approximation for $w_{\mathrm{el}}(t)$. Therefore, the resulting *A*-compensated waveform becomes

$$u_{\mathrm{el}}(\tau) = \sum_{i=1}^{N} r_i w_s(\tau - \tau_i). \tag{3.26}$$

Equation (3.26) gives a new seismic section with relatively sparse, zero-phase reflections having correct times, amplitudes, and dominant periods of the principal attenuation-corrected reflectors. At the same time, the wavelet $w_s(t)$ underlying an ITD-deconvolved image may be strongly different from the actual source waveform. Therefore, the ITD is not a pure attenuation-correction procedure but a broader signal-enhancement filter with *A*-compensation capabilities.

ITD represents the seismogram as a superposition of non-stationary source wavelets modeled using an appropriate empirical attenuation model. Because of the use of an iterative data-fitting procedure in time domain, this approach can be viewed as a wavelet transform or matching pursuit algorithm based on modeling the source waveform propagating through the section. The ITD method detects reflections principally by their dominant-frequency components. Thus, the ITD operates in the most advantageous part of the spectrum and has lower sensitivity to frequencies at which signal is weak. By identifying the time of the signal, this method is able to recover all frequency components (Deng, 2017). On the other hand, frequency-domain deconvolution methods tend to lose the highest-frequency component in the noise due to restoring each frequency component separately.

As shown on data examples in Chapter 4, the ITD offers significant improvements in enhancing the resolution, equalizing the amplitudes, and flattening the spectra of reflections in

seismic images. As also illustrated in Chapter 4, ITD has the advantage of not boosting the high-frequency noise and it is less sensitive to the accuracy of the *Q* model.

3.7 *Q* Models

Q models are mathematical models that describe the Earth respond to the propagating waveforms. There are various *Q* models which are used for modeling the wave propagation in the medium. In this section I am summarizing the two of those models; Azimi's *Q* model, and Kjartansson's Constant *Q* model.

3.7.1 Azimi's *Q* Model

Azimi *Q* model is one of the popular *Q* models. It suggests that the attenuation coefficient is proportional to the frequency at frequencies below the reference frequency ω_r and becomes near-constant above this frequency. Azimi *Q* model satisfies causality, and the attenuation coefficient can be described as:

$$\alpha(\omega) = \frac{a_1 |\omega|}{1 + a_2 |\omega|}, \tag{3.27}$$

where $a_1 = \frac{3}{4V_r Q_r}$, and $a_2 = \frac{1}{|\omega_r|}$, and ω_r is the reference frequency. The inverse phase velocity for this model equals:

$$\frac{1}{V(\omega)} = \frac{1}{V_r} - \frac{2a_1}{\pi} \ln(a_2 \omega) \tag{3.28}$$

and the *Q*:

$$Q(\omega) \approx \frac{1}{2a_1 V_r} - \frac{1}{\pi}\ln(a_2\omega). \tag{3.29}$$

Figure 3.8 Shows the attenuation and phase velocity and *Q* profile in Azimi *Q* model. As mentioned above, the attenuation $\alpha(\omega)$ is proportional to the frequency in almost linear trend at seismic frequencies.

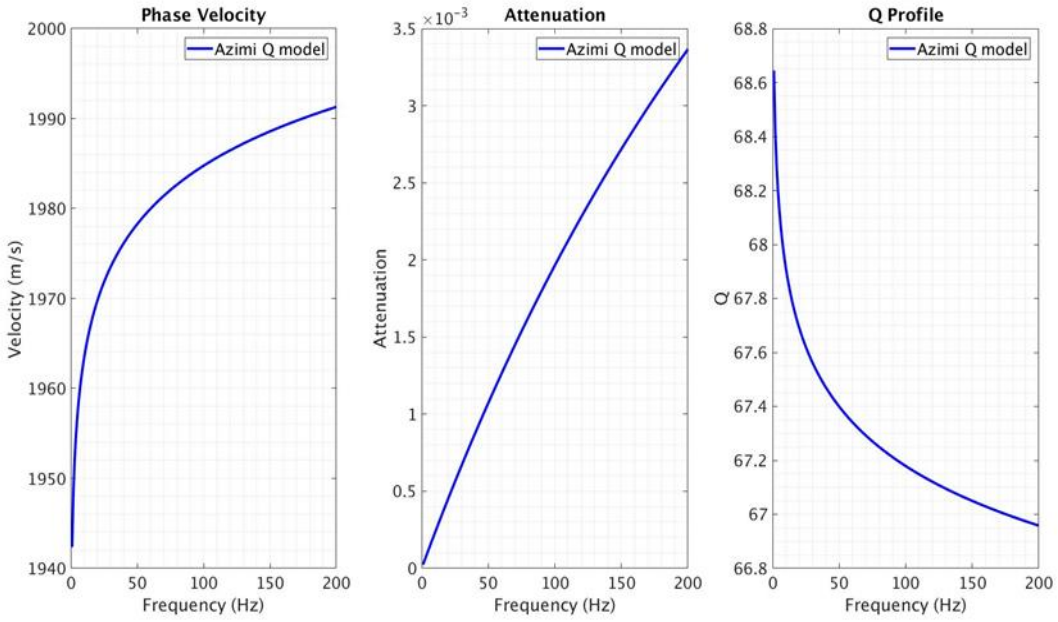

Figure 3.8 Azimi *Q* model

3.7.2 Kjartansson's Constant *Q* Model

The constant-*Q* theory of Kjartansson is considered as the simplest attenuation theory. It suggests that *Q* factor is of the frequency, and the phase velocity at the reference frequency is zero. The constant-*Q* attenuation given by Kjartansson (1979) is described as:

$$\alpha(\omega) = a_3 |\omega|^{1-\gamma} \tag{3.30}$$

The phase velocity:

$$\frac{1}{V(\omega)} = a_3 |\omega|^{-\gamma} \cot\left(\frac{\pi}{2}\gamma\right) \tag{3.31}$$

The Q model:

$$Q(\omega) = \frac{1}{2}\left[\cot\left(\frac{\pi}{2}\gamma\right) - \tan\left(\frac{\pi}{2}\gamma\right)\right], \tag{3.32}$$

where the factor $\gamma = \frac{1}{\pi Q_r}$, and $a_3 = \frac{|\omega_r|^{\gamma}}{2Q_r V_r}$.

Figure 3.9 displays the attenuation, phase velocity, and Q profile for Kjartansson's constant-Q model

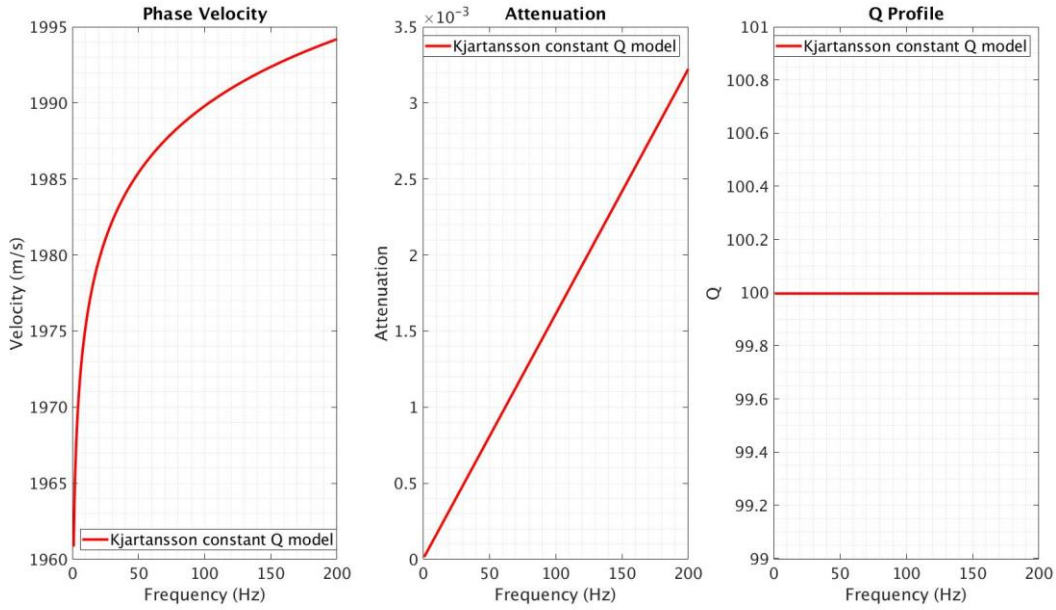

Figure 3.9 Kjartansson's Constant Q model

3.8 Discussion: Spatial Smoothness of *Q* Models

As argued by Morozov and Baharvand Ahmadi (2015) and Morozov et al. (2018), spatially smooth models are required for consistent interpretation of Q and modeling attenuation effects. Apparent-Q profiles always contain inherent averaging and cannot be accurately defined in the vicinities of boundaries (Deng and Morozov, 2017). The Q is simply not the type of property that can be measured and localized on both sides of a reflecting boundary. In particular, spatial variations of Q trade off with reflectivity and can hardly be consistently considered at reflection-time scales shorter than about 100 ms (White, 1992; Morozov and Baharvand Ahmadi, 2015). This shows that if reflection-time dependent $Q(t)$ is used for Q compensation, the Q relation should be smooth. As argued by Morozov et al. (2018), the same argument about spatial smoothness applies to empirical phase-velocity profiles $V(t)$ required for dispersion corrections. This analogy is easy to understand because by eq. (3.1), V and Q simply represent the real and imaginary parts of the complex phase velocity V^*.

Viscoelastic Q-factors attributed to the material are often arbitrarily detailed (Blias, 2012; Wang, 2008), but in almost all realistic cases, the Q is only a limited approximation for true mechanisms of internal friction. This approximation works for uniform media but is not guaranteed near boundaries. For example, in a layered poroelastic medium (Biot, 1956), slow waves are present near all boundaries, but these waves are not accounted for in the Q-based approximation. These slow waves contribute to reflectivity, and therefore the reflectivity from poroelastic layering differs from the one in a Q model (Morozov, 2015). Furthermore, in most cases, reflections from Q variation cannot be removed by Q-compensation due to the fact that it

would still contain time averaging in local Fourier transform (Hale, 1982), or inverse-Q filter (Wang, 2008).

For a simple argument showing that Q and phase-velocity models cannot be arbitrarily spatially detailed, consider, for example, the case of full-waveform inversion (FWI). In FWI, detailed, wavelength-scale variations of Q are often obtained (Prieux et al., 2013; Wang, 2008). However, because the spatial sampling of the model is always less dense than that of the recorded waveforms, FWI always requires regularization of the inverse problem and selection of optimization strategies (Prieux et al., 2013). It is easy to see that if a FWI is formulated on a very finely sampled grid of elastic moduli and density without regularization, then it should always be able to reproduce any input wavefield by using pure elastic modeling, i.e. with $Q^{-1} = 0$. For 1-D, this observation is rigorously illustrated by Deng and Morozov (2017), who show that Q-contrasts inverted from reflection records can always be explained by thin elastic layering and vice versa. Therefore, a short-scale variation of attenuation of Q^{-1} can always be interpreted as thin-layer reflectivity of the same relative magnitude. Also, because of the necessary use of regularization and optimization, FWI does not predict the recorded wavefield exactly, and the corresponding reflectivity error should be of the same order as the apparent Q^{-1}.

Thus, in FWI-based as well as in any finely-sampled velocity/density model, there is a fundamental trade-off between subwavelength-scale velocity variations and Q values. This trade-off is due to the nature of seismic Q (it is representing the complex part of phase velocity). To remove this trade-off, Morozov and Bahrvand Ahmadi (2015) recommended using only smoothly-varying Q models.

CHAPTER 4

APPLICATIONS OF ATTENUATION CORRECTIONS TO SEISMIC DATASETS

In this Chapter, I apply the inverse attenuation-filtering algorithms described in Chapter 3 to two stacked reflection datasets from Western China and provided by PanImaging. The first dataset is the 2-D seismic line which I described and processed in Chapter 2. The second dataset was provided already in the form of a stacked section by PanImaging. The goal of these examples is to illustrate the *A*-compensation approach for different data, different types of attenuation models, noise environments, and particularly to analyze the results of using the ITD and conventional Wiener deconvolution approaches.

This Chapter represents an expanded version of on my contributions to the following published paper:

- *Morozov, I., Haiba, M., and Deng, W., 2018, Inverse attenuation filtering: Geophysics, 83, no. 2, p. V135–V147.*

The copyright for this paper belongs to the Society of Exploration Geophysicists, which allows authors using their papers in their theses. Compared to the above paper, additional descriptions of the model and examples were added in this Chapter.

In the following section 4.1, I start by presenting the results of applying *A*-compensation to the first (pre-stack) dataset described in Chapter 2. This example was not included in the paper

above (Morozov et al, 2018). In section 4.2, I similarly describe the results with the dataset received in stacked form.

4.1 Pre- stack Dataset

This data set has a record length of 3000 ms. As described in Chapter 1, this dataset is hampered with significant noise, which was interpreted as caused by near-surface attenuation and strong surface waves. These effects could be due to recording over the very soft sedimentary rocks of the Loess Plateau in China. During the processing stage, I had to apply several filters specifically to reduce the effects of surface waves.

Spectral analysis of the seismic data shows that the dominant frequency within the shallow part of the data is about $f_{\text{dom}} \approx 25$ Hz. This frequency is used as the reference frequency $\omega_r = 2\pi f$ in dispersion relations. Unfortunately, no acoustic logs or laboratory data are available for both datasets, and therefore, it seems impossible to determine the accurate velocity dispersion law. Even with the availability of acoustic logs, velocity dispersion would be difficult to constrain. As shown by Deng and Morozov (2017) and at the end of Chapter 3, attenuation and dispersion effects on reflections trade off with layering thinner than about a quarter of the dominant wavelength, and this layering is impossible to determine from seismic data. In other words, the reflectivity can always be somewhat "colored," which may affect the Q and particularly the phase-delay spectra. Figure 4.1 shows the original seismic section before applying the inverse attenuation-filtering. The tapered time windows are displayed on the section

diagonally for better display. The length of those time tapers depends on the length of the waveform used in the convolution process.

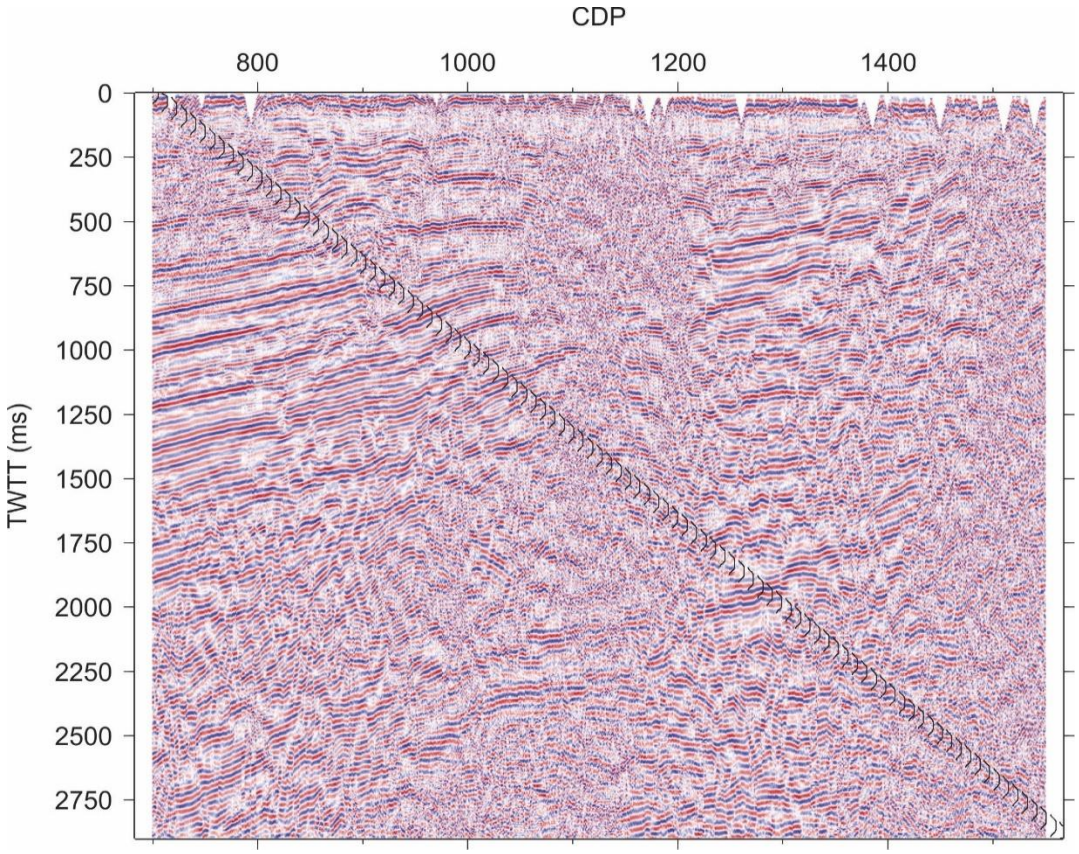

Figure 4.1 Color display of the stacked seismic section derived in Chapter 2 (Figure 2.12), with tapered time windows used in *A*-compensation shown along the diagonal.

In the following subsections, I describe several *A*-compensation tests using several useful forms of attenuation models and deconvolution approaches in IGeoS tool 'acomp'. In all cases, the depth models are parameterized by two-way normal-incidence times t_0. The r.m.s. velocity profile was derived from the results of seismic processing (Chapter 2) as a function of two-way

reflection time $V_{rms}(t_0)$ and transformed into interval velocities $V_{int}(t_0)$ within the processing job (Appendix A). Attenuation corrections are conducted within individual trace records, by using identical sets of overlapping tapered time windows shown in Figure 4.1

4.1.1 Constant *Q*, Wiener Deconvolution

Figure 4.2b shows the result of applying inverse attenuation filtering by using Kjartansson's (1979) constant-*Q* model with phase corrections (i.e., *Q* constant with frequency but varying with depth), and Wiener deconvolution. The *Q* profile was estimated from P-wave velocities using the relation suggested by (Li, 1993):

$$Q = 14V_p^2 \tag{4.1}$$

This transformation of *V* to *Q* was also performed by IGeoS tools placed above the 'acomp' tool in the processing job (Appendix A). A small zoomed-in portion of the resulting section is section is shown in Figure 4.2b. Compared to Figure 4.2a (the same fragment before applying inverse attenuation filtering), there is some improvement in terms of event details and sharpness.

The improvement of the records by attenuation corrections can be judged more accurately and quantitatively by the spectra of the signals at different depths. I measured the power spectra of the seismic section before and after attenuation filtering Figure 4.3 shows the spectra at two different depth levels: shallow (around 300 ms of two-way reflection time (TWTT); blue lines in Figure 4.3) and deep (near 2500 ms; red lines).

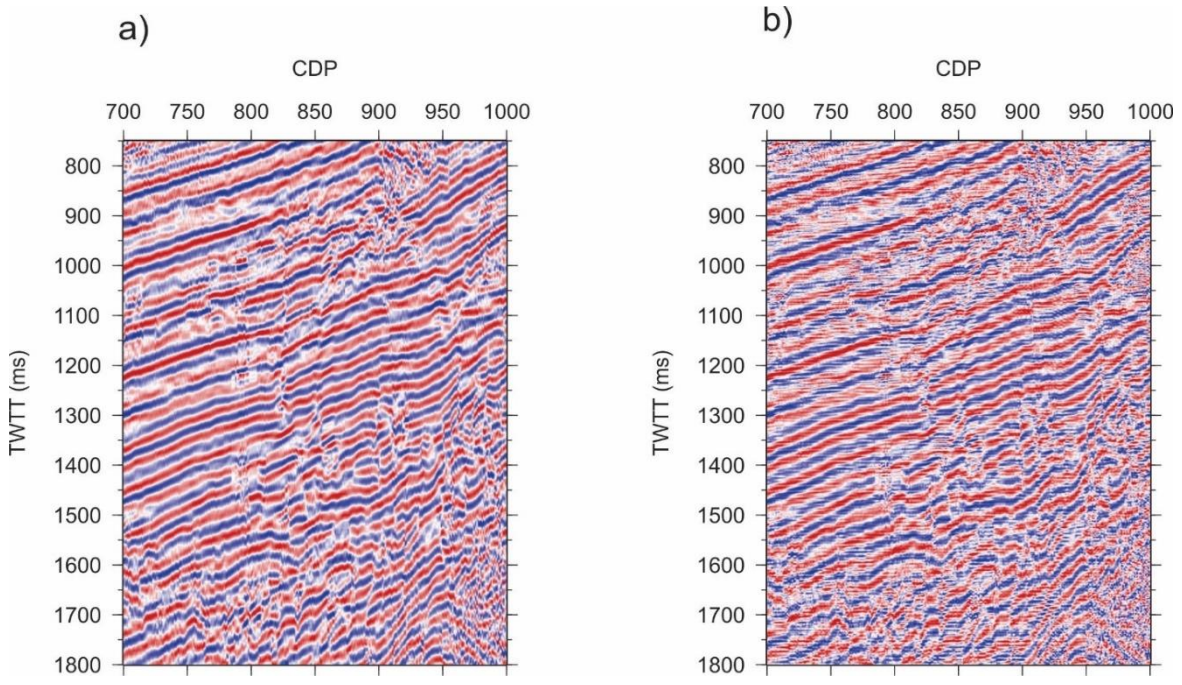

Figure 4.2 A comparison between original section a), and attenuation compensated section b) by inverse attenuation-filtering using constant *Q* model and Wiener deconvolution.

Dashed lines in this figure show the spectra before attenuation corrections, and solid lines show the spectra of corrected data. As seen from the differences between these lines at higher frequencies, the amplitude recovery of the deep part (solid lines) is significant and varying with frequency. Because prior to processing, the data are scaled by the amplitudes of the shallow part of the records, both input and the shallow output spectra (both dashed and red solid lines Figure 4.3) are close near the dominant frequency of the signal. Within the deep part or the records, the amplitude is increased (solid red line). In the shallow part, the amplitude is also increased at low frequencies (below about 15 Hz), which is not expected from Wiener *Q*-compensation but is likely due to the effects of the relatively short tapered windows. In any case, this increase leads

to flattening of the spectrum, which is a desirable effect. As a principal effect of *Q*-compensation, the spectra are boosted and flattened in the higher frequency ranges (60 to about 100Hz). However, between 100 and 140 Hz, an additional peak was created, particularly within the deeper part of the records (red line). This peak is likely caused by noise being boosted by *Q*-compensation. In subsequent processing and interpretation (not done in this Thesis), this part of the frequency band should be corrected by time-variant band-pass filtering.

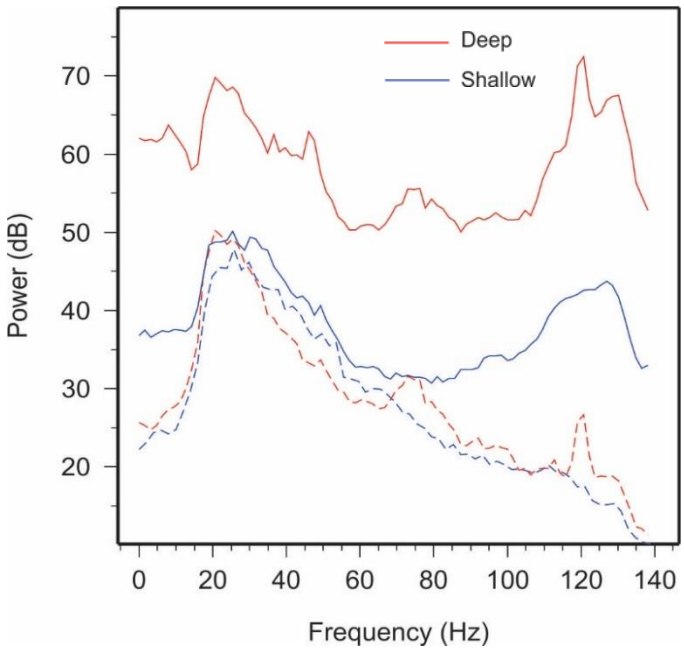

Figure 4.3 Averaged power spectra of the records before (dotted lines) and after Wiener deconvolution (solid lines) using the constant-*Q* attenuation model.

4.1.2 Azimi Attenuation Model and Wiener Deconvolution

Similar to the preceding subsection, Figure 4.4 shows a comparison between the original data (plot a), and the filtered result (plot b) by applying inverse attenuation filtering using the

Azimi's *Q* model (Chapter 2) and Wiener deconvolution. The results are improved in terms of events details and enhancing the resolution.

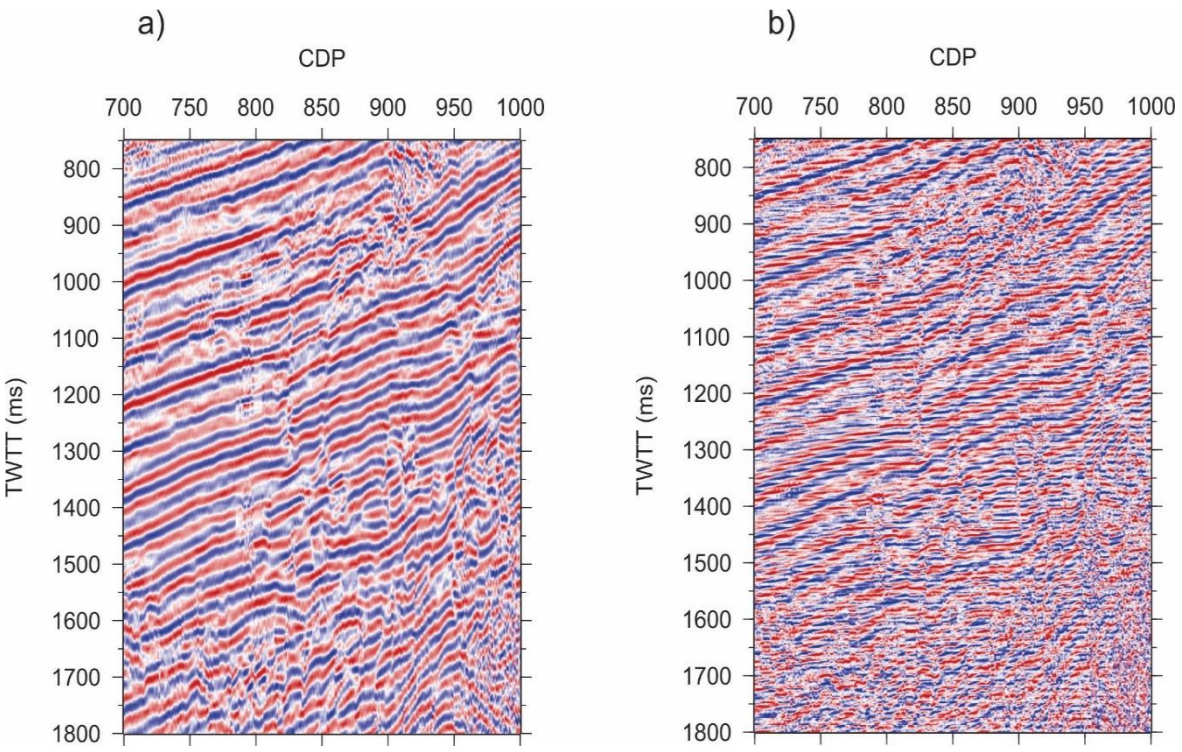

Figure 4.4 A comparison between original section a), and attenuation compensated section b) by inverse attenuation-filtering using Azimi model and Wiener deconvolution

The power spectra comparison Figure 4.5 shows a significant amplitude recovery. The decrease of the amplitudes with frequency (above approximately 30 Hz) is corrected, and the amplitude spectra are flattened within this frequency range. As in the preceding case, the average amplitudes of the deeper parts of the records are strongly increased by the attenuation-correction processing (solid red line in Figure 4.5).

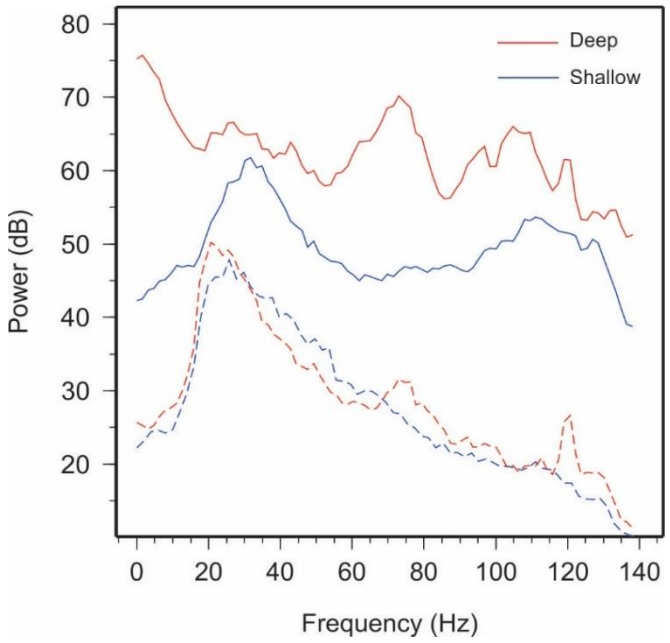

Figure 4.5 Averaged power spectra of the records before (dotted lines) and after Wiener deconvolution (solid lines) using the Azimi's *Q* attenuation model.

Also, as in the preceding subsection, an over-corrected peak, is present at frequencies above 130 Hz (Figure 4.3). This peak is likely caused by noise. Compared to the preceding example, the model shows a much stronger increase of high-frequency amplitudes and resolution. This increase occurs because of the *Q* decreasing with frequency in Azimi's model (Chapter 3), and therefore the *Q*-compensation gain is increased. However, this increase of gain also causes an increase of noise. The noise seems to lead to a peculiar "staircase" pattern in the output section (Figure 4.4b). This pattern is spurious and could be due to the spatial structure of this *Q* model. The model is defined at selected CMPs (those used in velocity analysis, Chapter 2)

and is constant between these CMPs. This is a drawback of the present algorithm (Appendix A), because as argued by Morozov and Ahmadi (2015) and Morozov et al. (2018), the *Q* model should always be smooth. The peculiar form of the "staircase" imaging artifact illustrates one kind of spurious "reflectivity" that can be produced by *Q* models with sharp horizontal contrasts. Generally, these results show high sensitivity of *Q*-compensation to this kind of *Q* models.

4.1.3 Amplitude-only *Q* Model and Attenuation Correction by ITD

To apply the ITD, an estimate of the source wavelet is needed, and I used a wavelet estimated from the upper part of the seismic section after an initial pass of Wiener inverse-*Q* filtering (subsection 4.1.1). By applying Wiener compensation, the wavelet becomes stationary (time-independent) and closer to the one originating from the source. By using the approximate *Q*-compensated section, I estimated the source wavelet in ProMAX by using the function called 'Derive Average Wavelet'. This function estimates the average wavelet for the entire data set. The method of this estimation consists in averaging the spectra of all traces within the specified time gate to produce the wavelet spectrum. By using this spectrum, the algorithm offers options to construct a zero, minimum-, or averaged-phase time-domain waveforms.

Figure 4.6 shows a detailed comparison between a fragment of the original dataset and the same ITD-filtered dataset. In Figure 4.6b, there are significant improvements in several areas. The vertical and horizontal resolution of the image is improved significantly, the reflectors are sharp and have more details without boosting the high-frequency components, and there is no spurious "staircase" pattern and over-boosting of the noise.

The power spectra of the result. (Figure 4.7) also show a significant enhancement. After inverse attenuation-filtering, the spectra flatten at higher frequencies without noise or windowing effects (Figure 4.7). Significant amplitude recovery and flattening of the spectra are achieved across the entire frequency band. The ITD boosted the high-frequency spectra for both shallow and deep parts of the records.

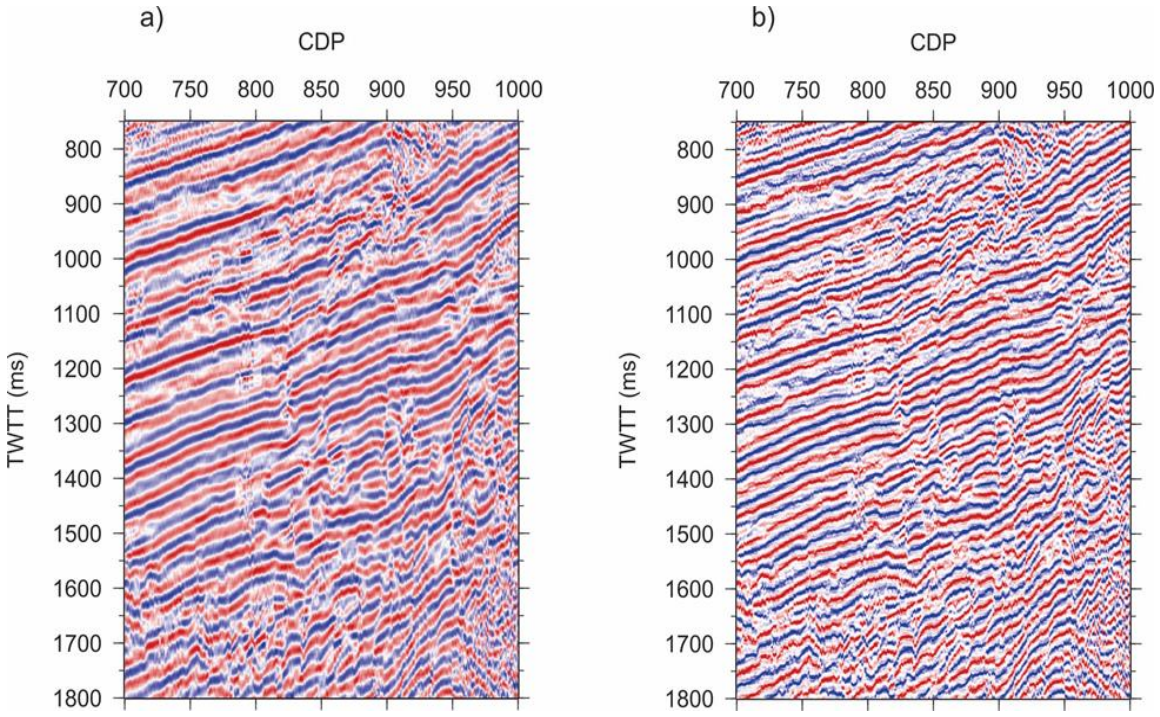

Figure 4.6 A comparison between original section a), and attenuation compensated section b) by inverse attenuation-filtering using *Q*-only model and ITD.

In contrast to the Wiener deconvolution results (preceding subsections), the average amplitudes of the resulting signals are close for ITD inversion (solid red and blue lines in Figure 4.7). This is because as mentioned in Chapter 3, the ITD is not an amplitude-correction but a signal-extraction procedure. After ITD, the average amplitudes and spectra of the outputs are

determined by the spectra of the source wavelet, and therefore they are close everywhere within the seismic section. Again, this is actually a desirable property for interpretation of seismic images.

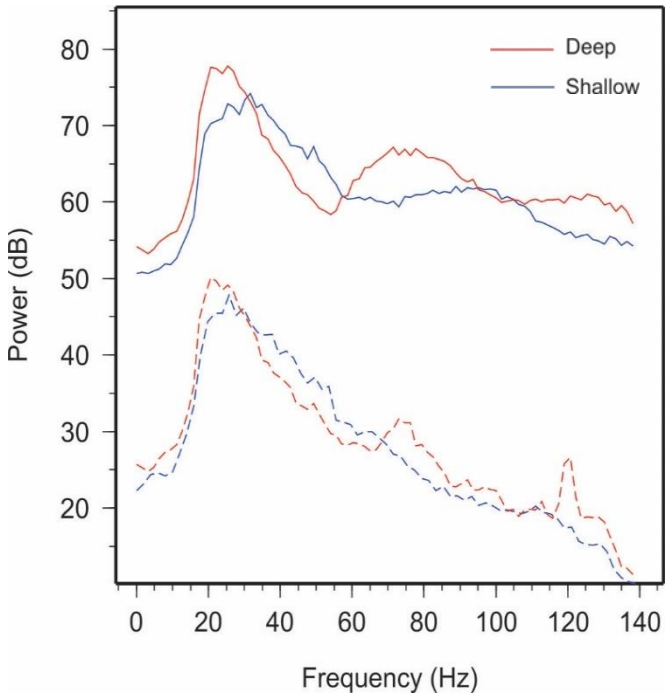

Figure 4.7 Averaged power spectra of the records before (dotted lines) and after Wiener deconvolution (solid lines) using the *Q*-only model and ITD.

4.2 Stacked Dataset

The second application of inverse attenuation filtering is made with the stacked reflection dataset provided by PanImaging. This dataset is dataset was used in data examples by Morozov et al. (2018). No acoustic logs were provided with these data, which prevent us to determine the

accurate velocity dispersion law. Here, as in Morozov et al. (2018), I use two fragments of the stacked section extracted from shallower (900–1700 ms two-way travel times) and deep (2500–4300 ms).

To this dataset, I applied two types of dispersion relations: the constant-*Q*, and the solid viscosity model (Chapter 3). The values of *Q* in these tests (Table 4.1) were established by trials and modified to achieve the best improvement of the stacked records and the spectral slopes of reflectivity spectra measured at several depths. Figure 4.8 shows the shallow part (a) and deep

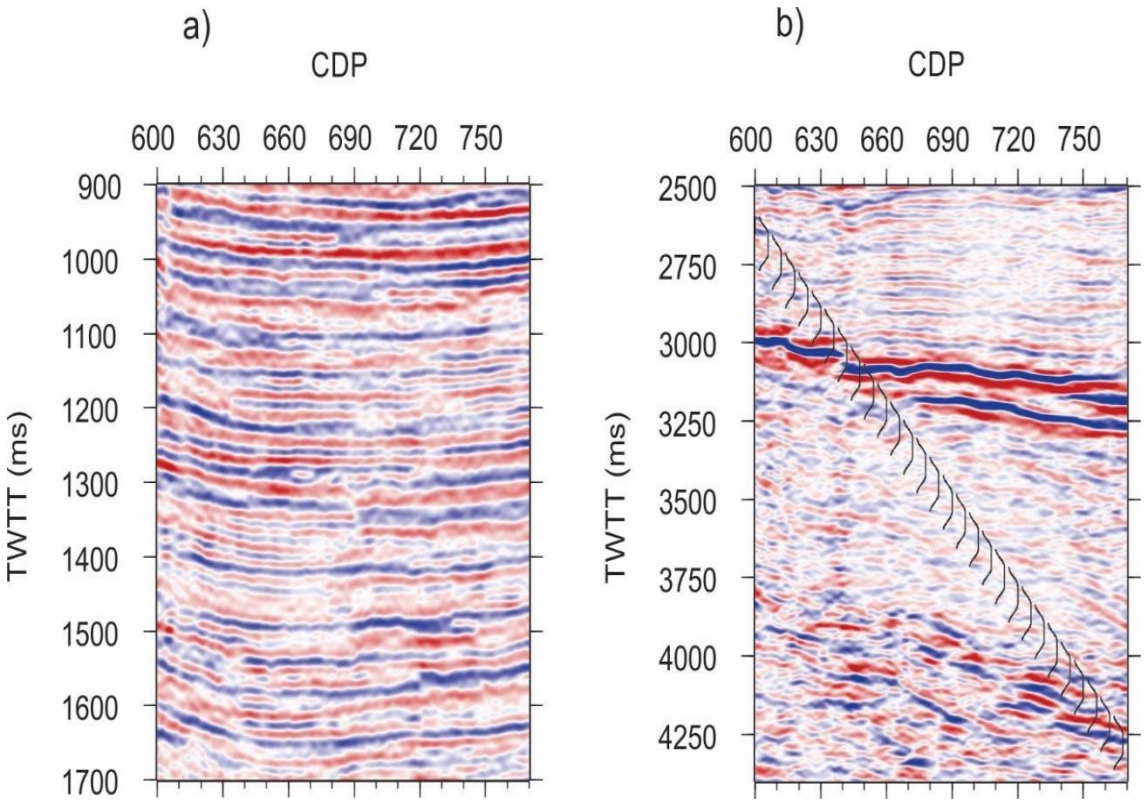

Figure 4.8 a) Shallow and b) deep portions of the stacked section used in inverse-attenuation filtering examples. Black lines in plot b) show the overlapping taper functions used for windowing the data.

part (b) of the original dataset before applying our method. Black lines in Figure 4.8b displays the overlapping taper function used for widowing the data. All of these widows belong to every trace but are shown as horizontally separated for clarity.

Table 4.1 Velocity and *Q* model used in field data examples

Two-way time (ms)	Interval velocity (m/ms)	*Q*
300	1.650	70
1000	2.100	70
2000	2.370	90
3000	2.900	140
4000	3.335	190
5000	3.570	190

Spectral analysis of this dataset shows that the dominant frequency is about 55 Hz. This frequency is used as a reference frequency in the velocity dispersion relations. Similarly to the previous dataset (section 4.1), the source wavelet was derived from the shallow part (around 100-200 ms TWTT) after applying initial inverse-*Q* filtering using a constant-*Q* model and Wiener deconvolution. The source wavelet was estimated in ProMAX by using the algorithm by Oppenheim and Schafer (1975) and assuming a zero-phase wavelet. Figure 4.9 shows the estimated wavelet (black solid line). The *Q* values in the selected zone for estimation are relatively low, and therefore, there is a significant attenuation causing the estimated wavelet to be somewhat narrow-band and reverberatory. To overcome these effects, a simplified Gaussian

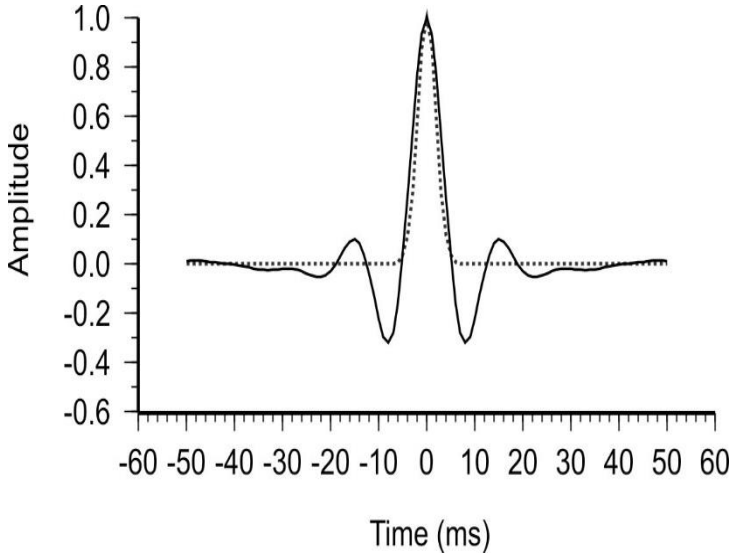

Figure 4.9 Derived source wavelet from-compensated record (solid line) and a simplified Gaussian wavelet used for shaping in the time-domain deconvolution example (dotted line)

wavelet was constructed by approximating the main lobe of the extracted wavelet (dotted line in Figure 4.9). This Gaussian wavelet will be used later for ITD.

4.2.1 Amplitude-only Constant-*Q*, Amplitude-only and Zero-phase Wiener Deconvolution.

In this test, I consider only amplitude effect of the *Q* during forward modeling and disregard the dispersion (Chapter 3). Similar to the results of section 4.1, application of *A*-compensation (Figure 4.10) shows an improvement in resolution more noticeable in the deeper part compared to the original dataset Figure 4.8. This is equivalent to the results of conventional inverse-*Q* filtering.

A comparison of the averaged power spectra of the records before and after filtering is shown in Figure 4.11. There is a noticeable amplitude recovery and flattening of the spectra, particularly for the shallow part of the data within the displayed frequency band.

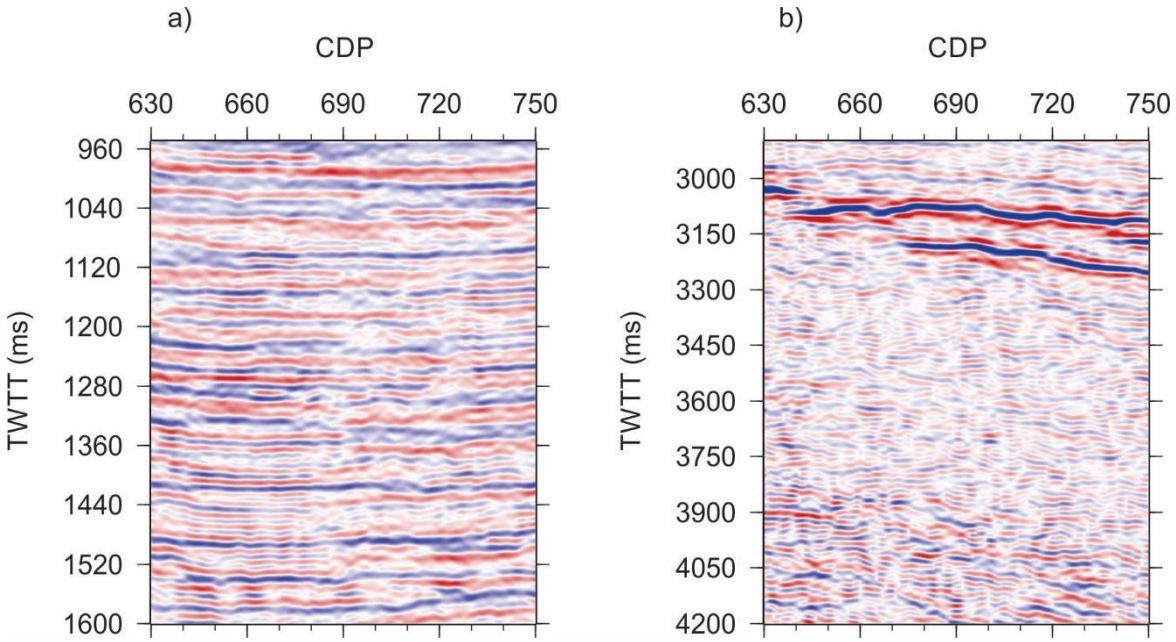

Figure 4.10 Attenuation-compensation using constant-*Q* model, amplitude-only corrections, and Wiener deconvolution a) shallow part of the record b) deep part of the record.

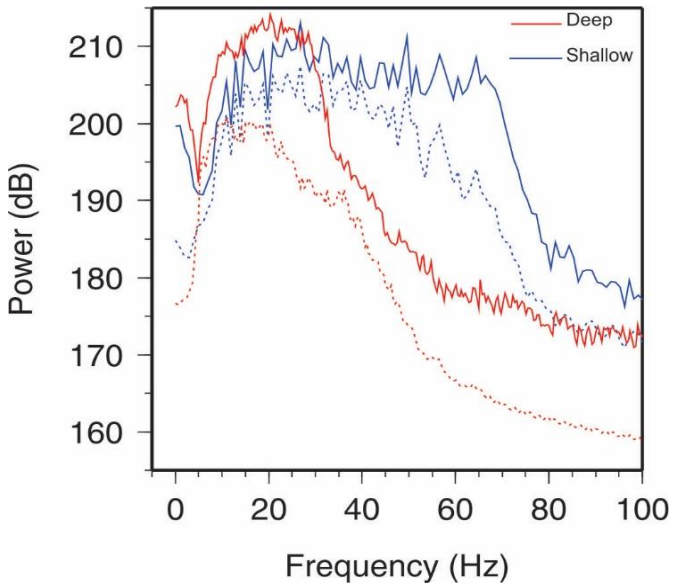

Figure 4.11 Averaged power spectra of the records before (dashed lines) and after Attenuation-compensation using constant-*Q* model, amplitude-only corrections, and Wiener deconvolution (solid lines).

4.2.2 Full Constant-*Q* Model and Zero-phase Wiener Deconvolution.

In this test, I use the full attenuation/dispersion constant-*Q* model, similar to the case of subsection 4.1.1.The results (Figure 4.12) show improvements of the images in terms of the appearance of the weak reflection, particularly in the deeper parts. The resolution of the section is also enhanced compared to the original dataset. The differences from using the amplitude-only model (Figure 4.10) are small but noticeable.

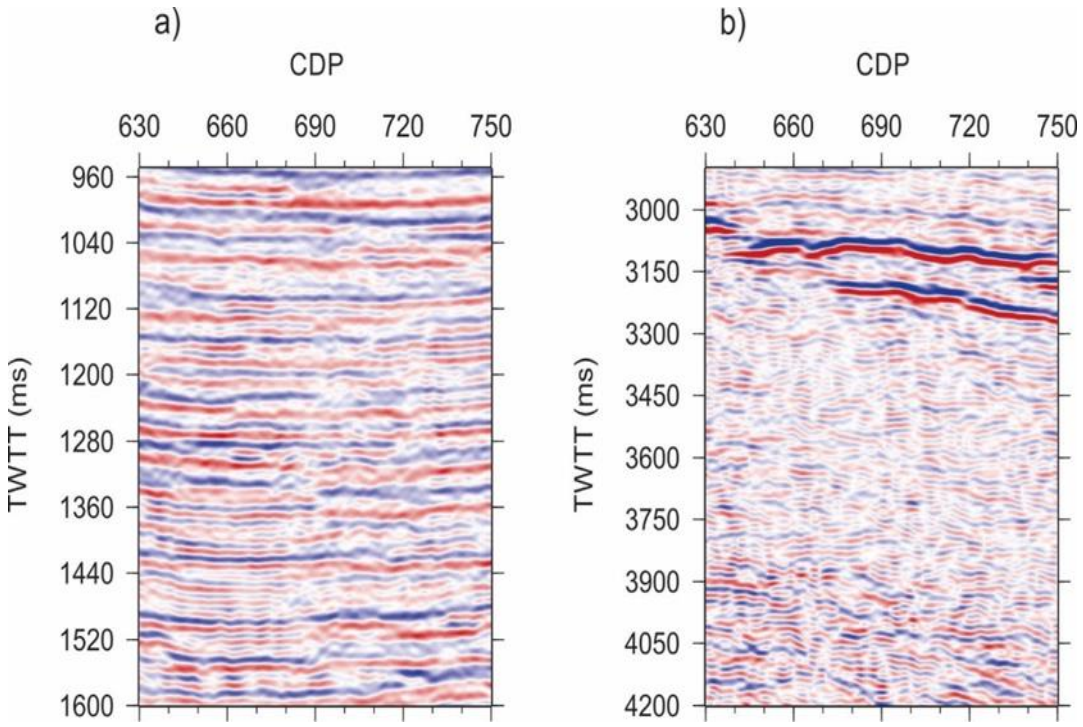

Figure 4.12 Attenuation-compensation using Kjartansson's constant-*Q* model, and Wiener deconvolution: a) shallower portion of the record; b) deeper portion

Figure 4.13 compares the spectra of the data before and after the inverse attenuation-filtering. For the shallow depth spectra (blue line), there is a noticeable amplitude recovery and significant flattening of the spectra, especially between 20 Hz to 70 Hz. The amplitude decrease with reflection time is also reduced. For the spectra of the deeper records, the spectral flattening is significant across the entire useable frequency band (approximately 10–60 Hz for such large depths). The flattened portion of the amplitude spectra extends to about 40 Hz. This improvement appears to be good, although it is of course not as significant as for the shallow parts of the records.

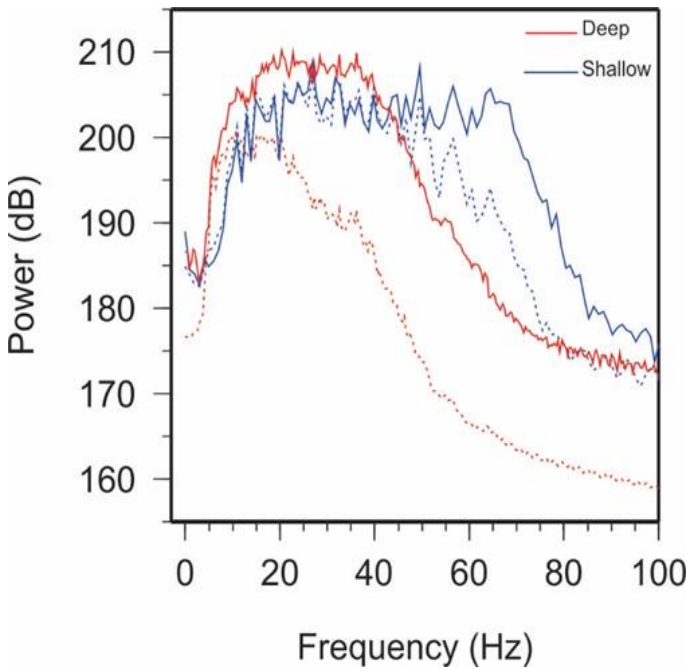

Figure 4.13 Averaged power spectra of the records before (dashed lines) and after Attenuation-compensation using Kjartansson's constant-*Q* model, and Wiener deconvolution (solid lines).

4.2.3 Solid-viscosity Attenuation Model and Wiener Deconvolution.

The next test examines the case of a solid-viscosity model implemented by Q inversely proportional to frequency (Chapter 3). The results in Figure 4.14 show improvement in the deep portion showing weak reflection and sharp details. High frequencies are gradually amplified in the solid-viscosity model stronger than in the constant-Q model. This is shown by increased high-frequency reflectors within the shallow part of the section (Figure 4.14a). However, these reflections also become reverberatory and may be over-gained.

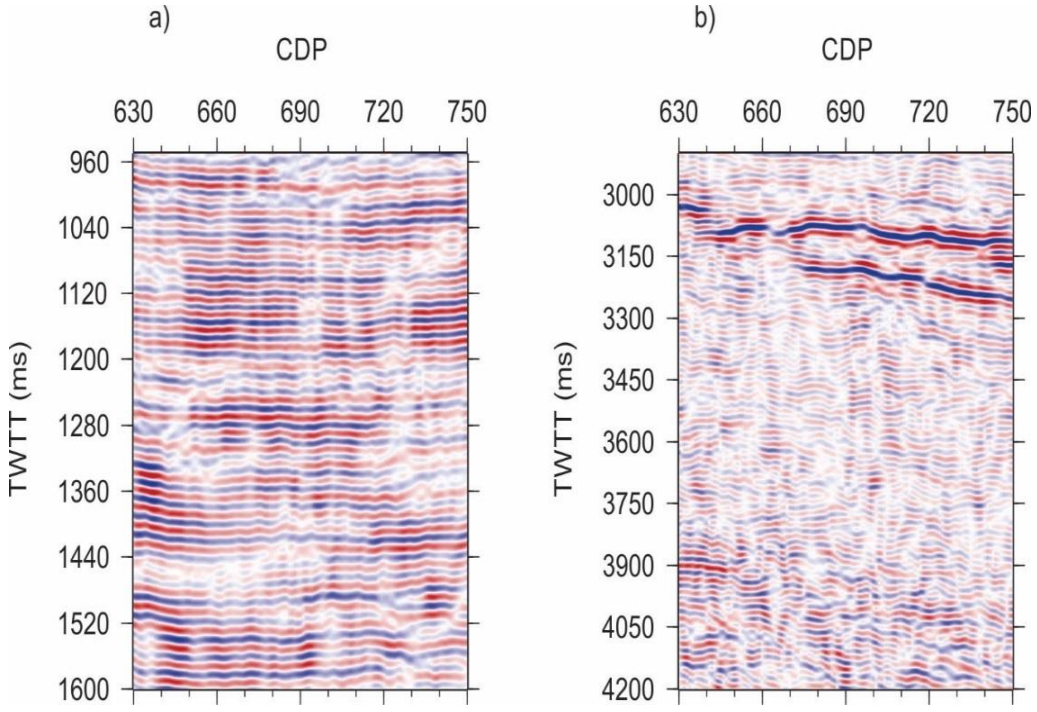

Figure 4.14 Attenuation-compensation using the solid-viscosity model and Wiener deconvolution: a) shallower portion of the record; b) deeper portion

The power spectra of the results (Figure 4.15) show strong enhancement of high-frequency amplitudes. Figure 4.15. also show that the spectra at shallow depths are boosted stronger than those at large depth.

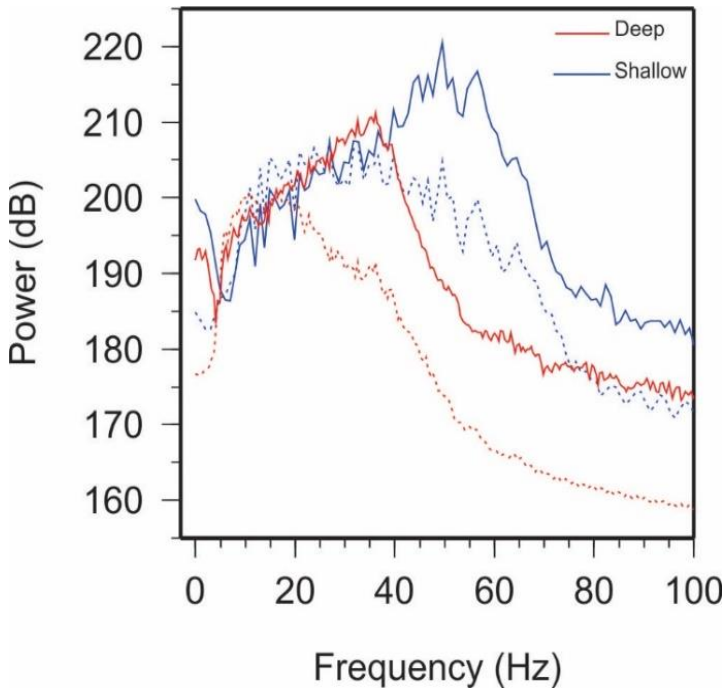

Figure 4.15 Averaged power spectra of the records before (dotted lines) and after Wiener deconvolution (solid lines) using the solid-viscosity model.

4.2.4 Amplitude-only Constant-*Q* Model and ITD

Finally, I test a constant-*Q* model, amplitude-only forward modeling, and iterative time-domain deconvolution (ITD). The ITD method is less sensitive to the accuracy of *Q*-model and to the estimated source wavelet. Compared to the preceding cases, the results in Figure 4.16 show significantly different images compared to Figure 4.12. The resolution, event details and

sharpness are improved, particularly in the deeper parts of the seismic section. The ITD appears to recover more reflectors and enhance their sharpness, and the signal to noise ratio appears to be also improved.

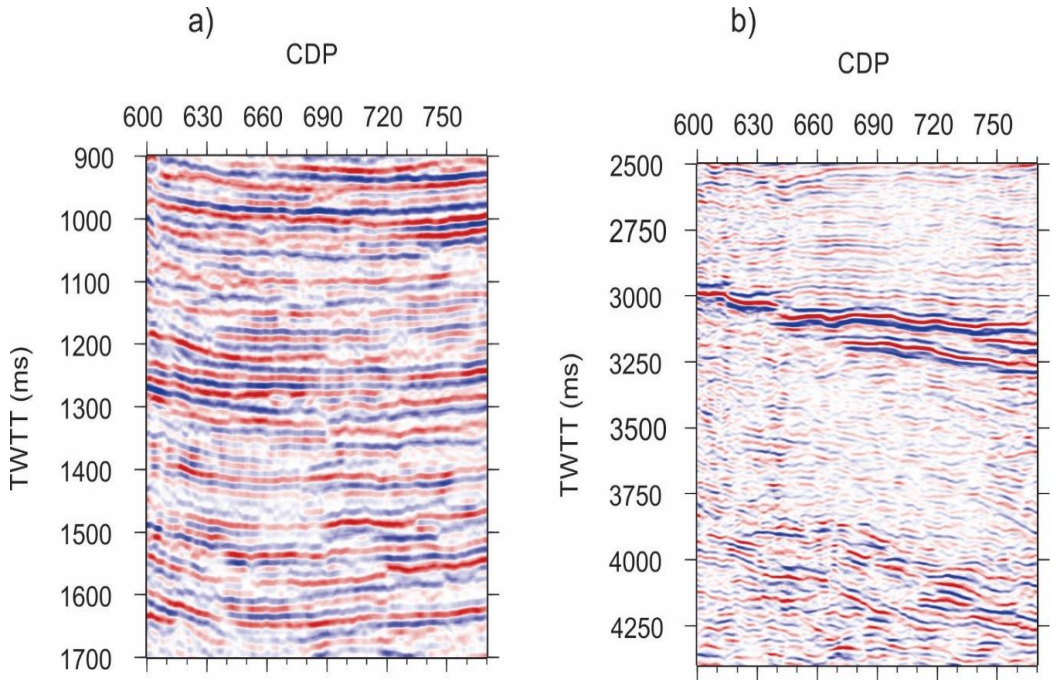

Figure 4.16 Attenuation-compensation using a constant-*Q* model, amplitude-only corrections, and iterative time-domain deconvolution: a) shallower portion of the record; b) deeper portion

Figure 4.17 compares the average spectra of the data before and after applying the inverse attenuation-filtering. Prior to this filtering, the high-frequency components starting at 40 Hz for the deep part and 60 Hz for the shallow part steeply decay with reflection time. These decays can be seen by increasing vertical distances between the red and blue dashed lines in Figure 4.17.

The ITD *A*-compensation procedure boosted the high-frequency components for both shallow and deep parts to close levels. For the shallow part (blue lines) the recovered spectrum is close to that of the shaping wavelet. The spectral recovery is significantly better than in the results using Wiener deconvolution and constant *Q* model (subsections 4.2.1 and 4.2.2). For the deeper part of the section (red lines), the *A*-compensation provides strong enhancement of the spectra and good flattening of the spectra.

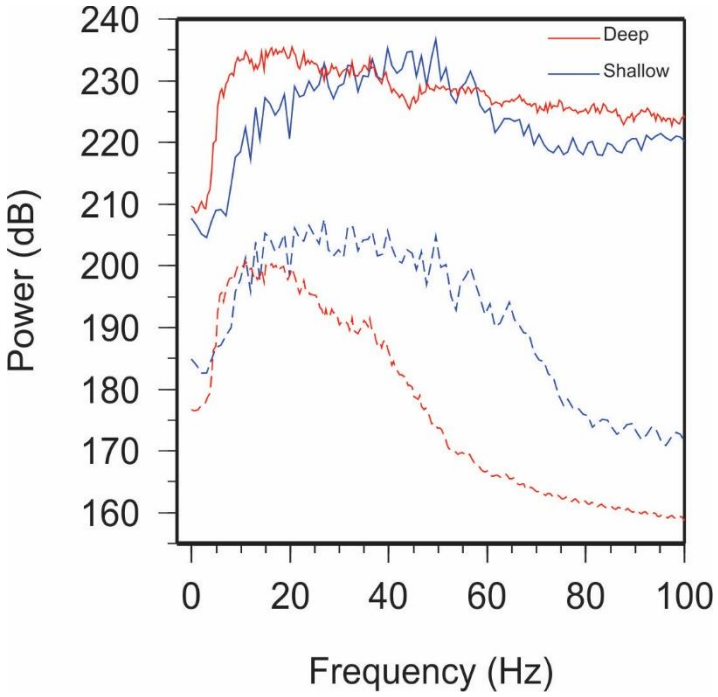

Figure 4.17 Averaged power spectra of the records before (dashed lines) and after ITD (solid lines) using a constant-*Q* attenuation model.

CHAPTER 5

CONCLUSIONS

This Thesis illustrates that modeling of attenuation effects and correction for them in seismic data is a much broader problem than the traditional forward and inverse *Q* filtering. Within the limited exploration-seismic frequency band, velocity dispersion relations can be relatively independent of the *Q*, and therefore independent amplitude and dispersion corrections need to be considered.

In addition to the phenomenological (apparent) *Q*, several non-*Q* type effects can and need to be included: focusing and defocusing of wavefronts (variations of geometric spreading), forward- and back-scattering, solid viscosity, and potentially, pore-flow related effects. In particular, solid viscosity studied on the examples of this Thesis appears to be a broad phenomenon that should be present within the Earth at all scales. At the same time, strong increase of attenuation with frequency requires accurate measurements of new properties of the medium, such as its solid viscosity.

For all types of attenuation and velocity dispersion mechanisms, corrections for their effects on seismic reflection records can be performed by modeling the propagating wavelet during its two-way propagation and deconvolving it from the records. These applications were implemented in flexible and convenient processing flows in our IGeoS seismic processing system.

Inverse attenuation filtering is a general and powerful approach to correcting for the effects of decaying amplitudes and velocity dispersion in seismic records. Real-data examples show that the inverse attenuation filter is practical and achieves improvements in the resulting sections while offering variety of modeling and deconvolution choices.

The iterative time-domain deconvolution (ITD) method is particularly effective, and it should be useful in exploration seismic applications. This method enhances the resolution of the attenuation-corrected records. Based on the examples tested in this Thesis, this method appears to be superior to the deconvolution methods commonly used in *Q*-compensation.

5.1 Recommendations for Future Research

Seismic attenuation is a very common phenomenon in seismic wave propagation. Inverse attenuation filtering aims to remove the effects of the attenuation. Provided that the properties of the attenuation (*Q* or non-*Q* type) model is known, the A-compensation approach is relatively straightforward, and several approaches to deconvolution can be used (Chapters 3 and 4). Thus, the key difficulty in applying this method is in determining the attenuation model of the subsurface. This problem is also present in the difficulty in determining the quality factor *Q* and its frequency dependence in conventional *Q*-compensation, However, in *A*-compensation, we need to also investigate different types of attenuation, such as waveform focusing/defocusing and solid viscosity.

Measuring the *Q* factors and determination of the physical models of attenuation is beyond the scope of this thesis, but I think such investigations should lead to most a significant

improvement of results compared to the conventional constant-*Q* inverse attenuation filtering. It should be useful to try tying the *A*-compensation algorithms to some methods of measuring the *Q* factor. For example, the *Q* could potentially be measured by optimizing the outputs of ITD inversion. As criteria of such optimization, sparseness of reflectors and flatness of the resulting spectra of the records could be used.

An interesting extension of the ITD to the determination of the effective *Q* factor could be derived from a recent study of source waveform estimation by Wang and Morozov (2020). This approach is similar to ITD and derives the source waveform by using sparse, highest-amplitude peaks from the reflection record. According to Wang and Morozov (2020), by optimizing the shape of the resulting source waveform (its shortest durations lowest side lobes, and optionally minimum or zero phase) may allow obtaining the *Q* factor. Although maybe ambiguous as a measure of physical properties of the subsurface, this *Q*-factor might be optimal for *Q*-compensation.

In addition to utilizing optimization methods for the determination of *Q*, analysis of well logging data could provide useful information for improving the accuracy and efficiency of the methods of this Thesis. This improvement could be obtained by providing more accurate velocity models, better correlations of velocities to *Q*-factors, or possibly to other types of attenuation models.

LIST OF REFRENCES

Aki, K., and P. G. Richards, 2002. Quantitative seismology, 2nd Edition: University Science Books.

Arntsen, B., L. Wensaas, H. Løseth and C. Hermanrud, 2007. Seismic modeling of gas chimneys. Geophysics, **72,** SM251-SM259.

Azimi, S. A., 1968. Impulse and transient characteristics of media with linear and quadratic absorption laws, Izvestiya. Physics. of the Solid Earth**,** 88-93.

Blanch, J. O., J. O. Robertsson, and W. W. Symes, 1995, Modeling of a constant Q: Methodology and algorithm for an efficient and optimally inexpensive viscoelastic technique. Geophysics, **60**(1), 176-184

Blias, E., 2012. Accurate interval *Q*-factor estimation from VSP data: Geophysics, **77**, no. 3, WA149-WA156, doi: 10.1190/geo2011-0270.1

Deng, W., 2017. Mechanisms and Models of Seismic Attenuation (Doctoral dissertation, University of Saskatchewan)

Deng, W. and I. B. Morozov 2017. Trade-off of elastic structure and *Q* in interpretations of seismic attenuation. Pure and Applied Geophysics, **174,** 3853-3867.

Dunn, K.-J., 1987, Sample boundary effect in acoustic attenuation of fluid saturated porous cylinders: Journal of the Acoustical Society of America, **81**, 1259–1266, doi: 10.1121/1.394529.

Frazer, L. N., X. Sun and R. H. Wilkens 1997. Changes in attenuation with depth in an ocean carbonate section: Ocean Drilling Program sites 806 and 807, Ontong Java Plateau.

Journal of Geophysical Research: Solid Earth, **102,** 2983-2997.

Futterman, W. I., 1962, Dispersive body waves: Journal of Geophysical Research, **67**, 5279–5291, doi: 10.1029/JZ067i013p05279.

Hale, D. 1982. *Q*-adaptive deconvolution. In *SEG* Technical Program Expanded Abstracts *1982*, 82–83. Society of Exploration Geophysicists.

Hargreaves, N. D., and A. J. Calvert, 1991. Inverse *Q* filtering by Fourier transform: Geophysics, **56**(4), 519-527.

Kjartansson, E., 1979. Constant *Q*-wave propagation and attenuation: Journal of Geophysical Research **84**, 4737-4748, doi: 10.1029/JB084iB09p04737.

Landau, L., and E. Lifshitz, 1986. Theory of elasticity: Pergamon Press, Oxford. Li, H., W. Zhao, H. Cao, F. Yao and L. Shao, 2006. Measures of scale based on the wavelet scalogram with applications to seismic attenuation. Geophysics, **71,** V111-V118.

Margrave, G. F., 1998, Theory of nonstationary linear filtering in the Fourier domain with application to time-variant filtering: Geophysics, **63**, 244−259.

Morozov, I. B., 2008, Open-source software framework integrates data analysis: EOS, Trans. American Geophysical Union, **89**, 261-262.

Morozov, I. B. and A. Baharvand Ahmadi, 2015. Taxonomy of *Q*: Geophysics **80**(1): T41-T49, doi: 10.1190/GEO2013-0446.1

Morozov, I., M. Haiba and W. Deng, 2018. Inverse attenuation filtering. Geophysics, **83,** V135-V147.

Morozov, I. B.,2008. Geometrical attenuation, frequency dependence of *Q*, and the absorption band problem. Geophysical Journal International, **175,** 239-252.

Morozov, I. B., 2010. On the causes of frequency-dependent apparent seismological *Q*: Pure and Applied Geophysics, **167**, 1131–1146

Morozov, I. B. & W. Deng,2016. Macroscopic framework for viscoelasticity, poroelasticity, and wave-induced fluid flows — Part 2: Effective media. Geophysics, **81,** D405-D417.

Newman, P., 1973. Divergence effects in a layered earth: Geophysics, **38**, 481-488.

Prieux, V., R. Brossier, S. Operto & J. Virieux, 2013. Multiparameter full waveform inversion of multicomponent ocean-bottom-cable data from the Valhall field. Part 1: imaging compressional wave speed, density and attenuation. Geophysical Journal International, **194,** 1640-1664.

Reine, C., R. Clark, and M. Van der Baan, 2012. Robust prestack *Q*-determination using surface seismic data: I - Method and synthetic examples: Geophysics, **77**, no. 1, R45-R56.

Štekl, I., and R. G. Pratt, 1998. Accurate viscoelastic modeling by frequency domainfinite-difference using rotated operators: Geophysics, **63**, 1779–1794

Stewart, R. R., P. D. Huddleston & T. K. Kan, 1984. Seismic versus sonic velocities: A vertical seismic profiling study. Geophysics, **49,** 1153-1168.

Strick, E., 1967. The Determination of *Q* , Dynamic Viscosity and Transient Creep Curves from Wave Propagation Measurements*. Geophysical Journal of the Royal Astronomical Society, **13,** 197-218.

Sun, L.F., B. Milkereit, and D.R. Schmitt, 2009. Measuring velocity dispersion and attenuation in the exploration seismic frequency band: Geophysics, **74**, no. 2, WA113-WA122, doi:10.1190/1.3068426.

Wang, Y., 2008. Seismic inverse *Q* filtering: Blackwell.

Wang, Y., and I. B. Morozov, 2020. A simple approach to non-stationary source waveform estimation in seismic records, Geophysics, doi: 10.1190/geo2019-0133.1

White, R., 1992. The accuracy of estimating *Q* from seismic data: Geophysics **57**(11), 1508-1511, doi: 10.1190/1.1443218

Yang, X., T. Lay, X.-B. Xie & M. S. Thorne, 2007. Geometric spreading of P_n and S_n in a spherical Earth model. Bulletin of the Seismological Society of America, **97,** 2053-2065.

Yao, Q. 2013. Velocity dispersion and wave attenuation in reservoir rocks.

Yilmaz, O., 2001. Seismic data analysis: processing, inversion, and interpretation of seismic data. Society of Exploration Geophysicists.

Zhou, J., S. Birdus, B. Hung, K. H. Teng, Y. Xie, D. Chagalov, A. Cheang, D. Wellen and J. Garrity. 2011. Compensating attenuation due to shallow gas through *Q* tomography and *Q*-PSDM, a case study in Brazil. In *SEG* Technical Program Expanded Abstracts 2011, 3332-3336. Society of Exploration Geophysicists.

APPENDIX A

This Appendix contains a fragment of the IGeoS data processing job and a Unix shell script performing key tasks of data analysis and plotting described in Chapter 4.

A 1.1 IGeoS Processing Job

The IGeoS job is presented in the "Fortran"-style scripts formatted by using tabulation characters. This simple format was used by one of the most popular seismic processing systems in the past called DISCO, and it is also the primary format used in IGeoS. In the following script, various tools are invoked sequentially by statements "`*call`" and parameterized by multiple options shown after these calls. These tools perform all data processing and produce most data plots shown in Chapter 4 of this thesis.

```
#############################################################################
##    input previously modeled wavelet:
#############################################################################
*call load  acomp-wiener-gauss-2-8.sia
## store the wavelet in memory buffer 'waveforms':
*call store waveforms
*end  keep  # block these traces from passing further in the job
#############################################################################
##    Step 1: Form the required 1-D models
#############################################################################
#1-D RMS velocity column:
*call readtab     table vrms_tab    # read in the file as a database table 'vrms_tab'
cdp   integer     1                 # table arguments are called 'cdp' and 'time'
time  float 2
```

```
vrms  float                   # table entry is called 'vrms'
file  all   radial_dmo_residuals_smooth_RMS_pick.txt
*call pritab                  # test printout of the table
vrms_tab

#############################################################################
## Interval velocity column:
*call model1      vint_model
use   vrms_model        # for each CMP, take the profile from vrms_model
transf      vrms->vint        # transform it to interval velocities
#############################################################################
## Derive a reference velocity model from interval velocity.
## The reference velocity is the velocity Vr used in modeling dispersion.
*call model1      vref_model
linear      1.0         # constant = 1 (test)
## A new model for 1/Q:
*call model1      q_model
use   vint_model
transf      vp->q       14    2.2   # transform the values of Vp into 1/Q
attrib      freq        25    # frequency of the Q model

#############################################################################
##    Step 2: Start over with trace data input and processing
#############################################################################

## load data traces from SEGY file(s):
*call load  Q_TEST_PROMAX/FX_stack_before.segy

#############################################################################
      # attenuation modeling options. You can use multiple entries of each type:
#############################################################################
a-q   ampl  qonly const 20    q_model           1.0               # constant Q and no dispersion
#a-q  full  constq      const 20    q_model           1.0         # Constant-Q (Kjartansson's) model
#a-q  full  futter      const 20    q_model           vref_model  # using Kolsky's (Futterman) model
#a-q  full  azimi const 20    q_model           vref_model        # using Azimi's model
```

```
#a-q  full  powlaw      const 20    q_model           vref_model  0.1   # using power-law Q (Muller's)
model
#a-q  full  visc  const 20    q_model           vref_model        # using solid-viscosity model

################################################################################
# deconvolution parameters:
################################################################################
fband                         # time-variant frequency band (Ormsby-type)
0     15    20    120   240
2000  15    20    80    100
2700  15    20    60    65
decon zero  0.0   wiener      40                decsrc            # Wiener deconvolution

#decon      model       itd   40    40    0.05              # Iterative time-domain deconvolution
################################################################################
#output
################################################################################
output      decon             # output final deconvolved records
################################################################################
```

A 1.2 Plotting script

The following is an example of the Unix Bourne shell used for plotting. This script is invoked by the IGeoS script (section A 1.2) and contains calls to Generic Mapping Tools (GMT) producing the desired PostScript files of the image.

```
#!/bin/sh
gmtset PAPER_MEDIA letter
gmtset ANOT_FONT_SIZE 10 LABEL_FONT_SIZE 10 MEASURE_UNIT inch HEADER_FONT_SIZE 10

ps=PS/$2.ps

echo plot_gmt_region is '>'$plot_gmt_region'<'
echo plot_gmt_gridding is '>'$plot_gmt_gridding'<'

region=-R700/750/1000/1800r
proj=-JX2.5i/-3.5i

palette=-Crwb-1.0.cpt         # red-white-blue
#palette=-Crwbk-1.0.cpt       # red-white-black
#palette=-Ctest2.cpt          # custom palette

# example of making a custom palette:

colortable=jet                # color table
makecpt -C$colortable -D -Z -T-1/1/0.1 > test2.cpt

xyz2grd $region $plot_gmt_gridding $1/traces.xyz -G/tmp/temp.grd

psbasemap $region $proj -B:."$2": -K -Y1i -X1i > $ps
psbasemap $region $proj -Ba50f50:"CDP":/f50g100a100:"TWTT (ms)":WsNe -O -K  >> $ps

grdimage /tmp/temp.grd $region $proj $palette -V -O >> $ps
evince $ps  &
```